

Banner appropriate to article type will appear here in typeset article

Laminar and Turbulent Flow in Wavy Pipes under Strong Wall Modulations

I. El Mellas¹, J. J. Hidalgo¹ and M. Dentz¹

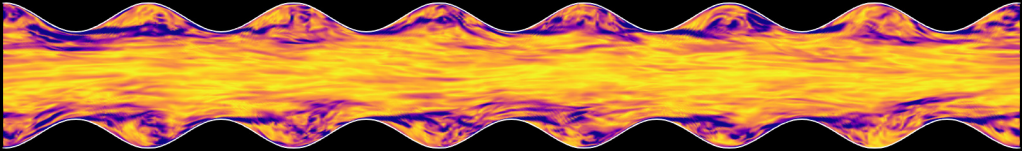
¹Spanish National Research Council (IDAEA-CSIC), Barcelona, Spain

Corresponding author: Marco Dentz, marco.dentz@csic.es, Ismail El Mellas, ismail.elmellas@idaea.csic.es

(Received xx; revised xx; accepted xx)

We investigate laminar and turbulent flow in pipes with periodically varying cross-sections, using direct numerical simulations over a range of Reynolds numbers between 1–5300. Pipe diameters are sinusoidally modulated in the axial direction, resulting in constrictions that reduce the local pipe radius by up to 40 percent. Such pronounced geometric roughness is encountered across disciplines, but is particularly relevant to karst systems, where dissolution-driven wall deformation leads to strong cross-sectional variability. Unlike classical roughness studies that assume small, homogeneous wall perturbations, the present configuration introduces large-scale axial variations that significantly affect flow structure, separation behaviour, and pressure drop even in the laminar regime. Once a critical roughness is exceeded, flow reversal appears at Reynolds numbers smaller than 25, inducing local recirculation zones and significantly increasing friction. These effects are not captured by classical models based solely on bulk geometric parameters, but require the definition of an effective hydraulic radius. Furthermore, the strong wall-induced mixing promotes an early transitions to turbulence in a Reynolds range between 500 and 1000, well below the classical threshold for smooth pipes. At higher roughness, the influence of Reynolds number becomes increasingly hidden by geometric effects, as the flow is dominated by inertial separation and wall-induced disturbances. The peak-to-peak amplitude provides a robust estimator for the equivalent sandgrain roughness. These findings emphasise the limitations of traditional friction laws in geometrically complex conduits and point to the need for new models that account for the interplay between large-scale roughness and inertial effects.

Key words: Pipe flow, turbulence, rough walls



1. Introduction

Most real conduits are neither straight nor smooth. Corrugated pipes, stented arteries, ventilation ducts and fractured rocks all show variations in cross-section, curvature and surface texture that alter flow resistance and mixing. Karst caves represent an extreme natural example: dissolution of limestone produces channels with irregular shapes and rough walls (Curl 1966; Dreybrodt 2012; Claudin *et al.* 2017). These geometric variations control head loss, solute transport and residence time, yet hydrological models still rely on empirical formulas derived for smooth pipes, such as the Hagen-Poiseuille law or the Darcy-Weisbach equation (Cohen & Kundu 2004). When roughness is considered, it is typically introduced through a relative roughness correction using the Moody diagram (Moody 1944), which assumes a uniform distribution of small-scale texture superimposed on an otherwise circular cross-section. This approach becomes increasingly unreliable when the roughness is large enough to alter the cross-sectional area itself, as is often the case in natural conduits. In such conditions, roughness is no longer just a wall property but a defining part of the overall geometry, and the underlying flow physics cannot be captured by standard friction factor correlations.

To isolate the influence of wall geometry, many studies use simplified rough-walled pipes. Such configurations allow systematic changes in roughness height, wavelength or curvature, providing a bridge between smooth, idealised models and the multiscale geometry of natural conduits. Many studies have aimed to define an equivalent sand-grain roughness height (k_s) to represent the effect of different surface roughness geometries. The equivalent sand-grain roughness height, k_s , introduced by Nikuradse (1933) and Schlichting (1936), remains the principal reference for quantifying wall friction. The non-dimensional roughness height is typically expressed in viscous units as $k_s^+ = k_s u_\tau / \nu$, where ν/u_τ is the viscous length scale, ν is the kinematic viscosity, and u_τ defined below.

Following Flack & Schultz (2014), flow is hydrodynamically smooth when $k_s^+ \lesssim 5$, transitionally rough for $5 \lesssim k_s^+ \lesssim 70$ and fully rough when $k_s^+ \gtrsim 70$. Roughness increases wall friction compared with smooth walls, but the mechanisms differ across these regimes: viscous damping dominates in the smooth regime, geometry controls drag in the transitional regime, and pressure drag governs friction in the fully rough regime, making it nearly independent of Reynolds number.

Compared to smooth surfaces, wall roughness enhances friction, which results in a reduced inner-scaled mean velocity profile. This reduction, referred to as the roughness function proposed by Clauser (1954) and Hama (1954), is typically expressed as:

$$\Delta U^+ = \frac{1}{\kappa} \log k_s^+ + A - B(k_s^+), \quad (1.1)$$

where $\kappa \approx 0.4$ is the von Kármán constant, and $A \approx 5$ is the smooth-wall additive constant, and B depends on the roughness geometry and k_s^+ (Jimenez 2004). As k_s^+ increases, the flow moves from the smooth to the transitional regime. When $\Delta U^+ > 7$, the flow is usually considered fully rough, and B becomes independent of Reynolds number. In wall-bounded turbulent flows, the velocity profile is typically separated into two regions: the inner layer, which is directly influenced by the wall and viscous effects, and the outer layer, where the dominant motions are larger in scale and relatively unaffected by the fine-scale details of

the wall. The inner layer includes the viscous sublayer, the buffer region, and the lower logarithmic layer, and its structure is strongly modified by roughness elements, particularly when their height in wall units, k_s^+ , becomes significant.

In contrast, the outer layer is assumed to become increasingly independent of wall characteristics as the Reynolds number increases. This is the basis of Townsend's outer-layer similarity hypothesis (Townsend 1976), which states that when there is sufficient scale separation (i.e., $k_s/\delta \ll 1$, where δ is the outer length scale of the flow, such as the pipe radius), roughness effects remain confined to the near-wall region. Under these conditions, the outer-layer turbulence retains a universal structure, and the effect of roughness manifests primarily as a downward shift in the mean velocity profile, quantified by an additive constant ΔU^+ , in the logarithmic law. However, this assumption may break down when the roughness becomes comparable to the boundary layer thickness or induces large-scale secondary flows that extend into the outer region (Jimenez 2004). Townsend's hypothesis has been shown to approximately hold across a variety of canonical roughness types, such as sand-grain roughness, cylindrical elements, and spherical particles (Flack *et al.* 2005; Chan *et al.* 2015; Busse *et al.* 2015, 2017). These studies, both experimental and numerical, represent roughness as small-scale geometric perturbations superimposed on otherwise smooth and straight channels or pipes, using idealised elements like hemispheres, ribs, or random sand-grain topographies (Jimenez 2004; Busse *et al.* 2015; Thakkar *et al.* 2016). These studies model roughness as small-scale perturbations superimposed on an otherwise straight conduit, idealised elements such as hemispheres, ribs, or sand-grain like particles.

More recent investigations have extended these works to irregular and stochastic roughness in both plane channels and pipes, exploring how roughness amplitude, spacing, and spatial arrangement modulate near-wall turbulence and affect the mean flow (Thakkar *et al.* 2018; De Maio *et al.* 2023). Parallel efforts have aimed to establish direct correlations between the equivalent sand-grain roughness height k_s and the underlying geometric characteristics of the roughness elements (Napoli *et al.* 2008; Chan *et al.* 2015; Saha *et al.* 2015; Forooghi *et al.* 2017; Flack & Schultz 2020). However, rough-wall models typically assume statistical homogeneity in the axial direction, with wall deformations treated as local surface features rather than large-scale geometric variations. In many natural systems, such as karst conduits, the geometry changes more fundamentally along the flow path, affecting the cross-section, curvature and flow alignment in ways that local roughness models cannot capture (Jeannin 2001).

To explore these effects in a simplified and controlled setting, a widely used configuration is the wavy pipe. It offers an intermediate step between rough pipes and fully irregular natural conduits that is able to reveal the salient features of the flow dynamics in natural conduits. Wavy geometries have been studied extensively in the context of compact heat exchangers and membrane oxygenators, where enhanced mixing and convective transport are desirable outcomes (Goldstein & Sparrow 1977; Wang & Vanka 1995; Wang & Chen 2002; Guzmán *et al.* 2009). Such studies introduce a periodic, global deformation of the conduit wall that alters both the mean flow and turbulence structure. Hsu & Kennedy (1971) and Nishimura *et al.* (1984) both examined flow through channels with sinusoidal walls, showing that wall waviness promotes vortex formation and increases pressure losses. The former focused on turbulent flow in wavy pipes, whereas the latter investigated steady, quasi-two-dimensional laminar flow. In both cases, the recirculating vortices that develop in the diverging sections raise wall shear and pressure drop. Pozrikidis (1987) studied creeping Stokes flow in two-dimensional periodic channels and demonstrated that flow reversal and recirculation can arise even at vanishingly small Reynolds numbers, with a strong dependence on the driving mechanism and channel shape. Complementing these

works, Nishimura (1995) carried out experiments on oscillatory flow and mass transfer in both asymmetric and symmetric sinusoidal channels, showing that the onset of unsteady oscillations markedly enhances mass-transfer rates.

The topic has also been investigated using numerical simulations, particularly in relation to heat transfer enhancement and flow performance in wavy or corrugated geometries. Studies such as Guzmán *et al.* (2009) and Sui *et al.* (2012) have shown that geometrically induced flow separation and bifurcations enhance mixing and thermal performance in periodic channels. Several numerical investigations, including Wang & Vanka (1995) and Wang & Chen (2002), have further demonstrated that periodic wavy walls can lead to flow unsteadiness and enhanced convective transport, particularly as Reynolds number and wall amplitude increase, although this comes at the cost of increased pressure drop.

Beyond heat-transfer applications, purely hydrodynamic studies include Wang & Du (2008), who used the lattice Boltzmann method to examine viscous flow in wavy pipes and observed secondary flows and enhanced pressure losses driven by curvature. Loh & Blackburn (2011) performed a linear stability analysis of steady flow in circular pipes with sinusoidal axial corrugations. They found that increasing the corrugation amplitude lowers the critical Reynolds number for the onset of instability, promoting earlier transition from stable to unstable flow. The most unstable modes are asymmetric or standing-wave-like, often localised near separation bubbles inside the corrugations. These findings suggest that wall waviness can significantly destabilise laminar pipe flow. Saha *et al.* (2015) analysed pipe flows over sinusoidal transverse corrugations and proposed scaling laws to quantify friction and flow structure across laminar to transitional regimes.

While these studies have advanced the understanding of flow behaviour in wavy or corrugated geometries, important gaps remain. In particular, most numerical investigations have focused on heat transfer applications, often relying on turbulence models. Direct numerical simulations (DNS) exploring strong geometric variations, especially at high amplitude-to-diameter ratios, are scarce. Moreover, few works have systematically examined how such geometries influence the transition from laminar to turbulent flow or how they modify momentum transport across regimes. The definition of an effective hydraulic diameter in non-uniform geometries remains ambiguous, complicating the use of conventional scaling laws. Similarly, attempts to quantify an equivalent sand-grain roughness height for globally deformed yet smooth walls are limited, leaving friction factor comparisons with canonical rough-wall data, such as Nikuradse's, on uncertain ground.

We address these open questions by analysing flow in circular pipes with axisymmetric wavy walls using DNS. The pipe radius varies periodically along the streamwise direction. The wall geometry is defined analytically, enabling controlled variation of roughness amplitude and wavelength while preserving a smooth, circular cross-section. The analysis spans laminar, transitional, and turbulent regimes to examine how wave-induced roughness influences flow development, pressure drop, and the onset of turbulence. Particular focus is given to the characterisation of wall friction and the definition of an effective sand-grain roughness height, enabling comparison not only with classical data such as Nikuradse's fully rough pipe measurements, but also with more recent studies involving controlled roughness geometries (Nishimura *et al.* 1984; Saha *et al.* 2015; De Maio *et al.* 2023), who examined higher roughness levels in random and wavy rough pipes. By varying Reynolds number and geometric parameters systematically, the study aims to clarify the role of large-scale, structured roughness in both momentum transport and flow regime transitions.

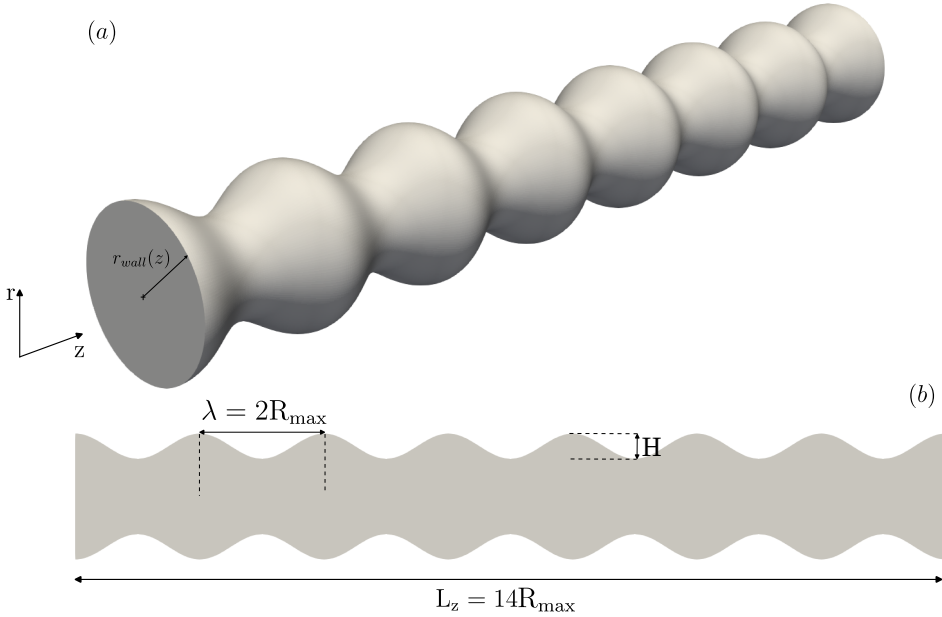


Figure 1. Schematic of the simulation geometry. (a) Three-dimensional view of the wavy pipe, where the wall radius varies periodically along the axial direction according to Eq. (2.1). (b) Longitudinal section illustrating one full wavelength and the total pipe length $L_z = 14R_{\max} = 7\lambda$. The flow is oriented along the z -axis. Periodic boundary conditions are imposed at the inlet and outlet, while no-slip conditions are applied at the pipe wall.

2. Methodology

In the following, we define the pipe geometry, state the flow equation and basic relations of pipe flow, and provide details of the direct numerical simulations (DNS).

2.1. Pipe geometry

We consider the wavy pipe geometry illustrated schematically in Fig. 1, which also defines the notation used in the following. The wall radius $R(z)$ measured from the straight centerline is given by the analytical expression

$$R(z) = R_{\max} - \frac{k}{2} \left[1 - \sin\left(\frac{2\pi z}{\lambda}\right) \right]. \quad (2.1)$$

Here R_{\max} is the maximum pipe radius, $k < R_{\max}$ is the peak-to-peak amplitude of the wall waviness, i.e., $k = R_{\max} - R_{\min}$, and λ the streamwise wavelength of the sinusoidal modulation. We fix here $R_{\max} = \lambda/2$ and vary R_{\min} to modify k . The baseline smooth pipe is characterised by the radius $R(z) = R_{\max}$. The average pipe radius is given by $\bar{R} = R_{\max} - k/2$. The cases considered in this work span the five values $k = 0, 0.0477\lambda, 0.091\lambda, 0.1304\lambda$, and 0.2λ , which correspond to $\bar{R}/k = 0, 10, 5, 10/3, 2$, see also Table 1. The variable pipe diameter is denoted by $D(z) = 2R(z)$.

Throughout this work, the terms waviness and roughness are used interchangeably, although the imposed geometry is smooth and periodic. The geometrical roughness height here is defined as the peak-to-peak wall amplitude, k . Other definitions for the wall roughness are discussed in Section 3.5. As emphasized by Jimenez (2004), roughness or equivalent sand-grain roughness is a hydrodynamic concept that reflects the impact of wall fluctuations on wall shear stress and flow resistance. A challenge here is to identify and relate the geometric wall characteristics to the flow resistance in the fully rough regime

(Chung *et al.* 2021), which is discussed in Section 3.5. In the following, we summarize a series of geometric surface statistics that have been proposed to characterize geometric roughness with the aim of correlating them to the hydrodynamic function of roughness.

Schlichting (1936) defines the solidity σ to characterize the surface geometry as the “total projected frontal area of a roughness element per unit wall-parallel projected area” (Jimenez 2004). For the wavy pipes under consideration here it is $\sigma = k/\lambda$. Napoli *et al.* (2008) propose the effective slope ES ,

$$ES = \frac{1}{\lambda} \int_0^\lambda \left| \frac{dR(z)}{dz} \right| dz, \quad (2.2)$$

as a measure that is equivalent to solidity, but simpler to use for random surfaces. In fact, the effective slope is two times the solidity $ES = 2\sigma$. That is, here $ES = 2k/\lambda$. Other authors (Chan *et al.* 2015; Forooghi *et al.* 2017; Flack & Schultz 2020) consider surface statistics of the roughness height fluctuation (Musker 1980), which here is simply

$$k'(z) = R(z) - \bar{R} = \frac{k}{2} \sin\left(\frac{2\pi z}{\lambda}\right). \quad (2.3)$$

These authors use the skewness S_k of the height fluctuation, which here is exactly zero, the root-mean square roughness S_q , which here is $S_q = k/2\sqrt{2}$, or the average absolute height S_a , which here is $S_a = k/\pi$.

2.2. Flow

The flow is given by the incompressible Navier-Stokes equations

$$\nabla \cdot \mathbf{u} = 0 \quad (2.4)$$

$$\frac{\partial \mathbf{u}}{\partial t} + \mathbf{u} \cdot \nabla \mathbf{u} = -\frac{1}{\rho} \nabla p + \nu \nabla^2 \mathbf{u}, \quad (2.5)$$

where $\mathbf{u} = (u_1, u_2, u_3)$ denotes the fluid velocity vector and velocity components in 1, 2 and 3-directions of the coordinate system, t the time and p the pressure. No-slip boundary conditions are applied at the walls of the pipe and periodic boundary conditions at the inlet and outlet. The bulk velocity u_b is imposed, which is defined as the spatial average of the time-averaged streamwise velocity u

$$u_b = \frac{1}{V} \int_{\Omega} u dV, \quad u = \frac{1}{T} \int_0^T u_1 dt, \quad (2.6)$$

where Ω denotes the flow domain, V its volume, and T the averaging interval discussed in Section 2.3.2 below. The bulk Reynolds number is defined in terms of the maximum pipe radius R_{\max} and the bulk velocity u_b as

$$Re_b = \frac{2R_{\max} u_b}{\nu}. \quad (2.7)$$

The pressure gradient $G = -\frac{dP}{dz}$ is a result of the solution of the Navier-Stokes equation. The wall shear stress τ_w is defined in terms of G , the friction velocity u_τ in terms of τ_w as,

$$\tau_w = \frac{R_{\max} G}{2}, \quad u_\tau = \sqrt{\frac{\tau_w}{\rho}}. \quad (2.8)$$

Note that we use the maximum pipe radius to define the wall shear stress. Note, however, that the wall shear stress varies in streamwise direction along the wavy pipe. The friction velocity u_τ is used to define the friction Reynolds number as

$$Re_\tau = \frac{R_{\max} u_\tau}{\nu}. \quad (2.9)$$

Furthermore, we define the roughness Reynolds number k^+ as

$$k^+ = \frac{k u_\tau}{\nu}. \quad (2.10)$$

It compares the geometric roughness height k and the viscous length scale $\delta = \nu/u_\tau$. For $k^+ \gg 1$, the wall roughness height is penetrating through the viscous wall layer. In this fully rough regime, wall shear stress becomes independent of viscosity. Wall friction is dominated by Reynolds stresses and turbulent pressure drag across the boundary layer. In the following, quantities that are rescaled in terms of wall units (velocities by u_τ , length by δ) are denoted by a superscript $+$.

2.2.1. Darcy friction factor

The global flow resistance due to wall friction is quantified by the Darcy friction factor. It is defined according to the Darcy-Weisbach formulation (White 2011)

$$f = \frac{4R_{\max}}{\rho u_b^2} G. \quad (2.11)$$

It can be rewritten in terms of the wall shear stress as

$$f = 8\tau_w / (\rho u_b^2). \quad (2.12)$$

The friction factor is used throughout this study as a global indicator of flow resistance. While in smooth-wall flows f depends primarily on Reynolds number, geometric modifications such as wall waviness introduce additional drag via enhanced turbulence production and form-induced pressure losses. The evolution of the friction factor with increasing Reynolds number and wall modulation will be used to quantify the hydrodynamic impact of waviness and to establish comparisons with classical rough-wall behaviour. Note, that here we define friction factor and wall shear stress in terms of the maximum pipe radius. These definitions will be revised in Section 3.4, where we discuss them in the light of an effective hydraulic diameter D_h .

2.2.2. Velocity statistics

In order to assess the impact of roughness on the turbulence intensity and the locations of turbulence production, we consider profiles of the mean streamwise velocities and the variances of the time-averaged streamwise, radial and angular velocity components, which are denoted in the following by $u_z = u$, u_r and u_θ . We denote the axial, radial and angular coordinates by z , r and θ , respectively.

Due to the variable wall geometry, we depart from the standard practice of averaging over the entire axial domain. The analysis of individual regions allows for the identification of local flow behaviours, such as recirculation and flow detachment, which would otherwise be obscured by a global average. Thus, we extract cross-sectional slices at selected streamwise locations that correspond to distinct geometric features of the wavy wall profile, as defined in (2.1). Specifically, we select contraction regions where the wall radius reaches its minimum, $R(z_i) = R_{\min}$, at $z_i = (2i - 1)\lambda/2$, expansion regions where the radius is maximal, $R(z_i) = R_{\max}$, at $z_i = i\lambda$, and intermediate regions where the radius takes the

average value $R(z_i) = \bar{R}$, at $z_i = (2i - 1)\lambda/4$. Thus, the average for each region along the pipe is defined by

$$\langle \phi \rangle_k(r) = \frac{1}{N_k} \sum_{i=1}^{N_k} \frac{1}{2\pi} \int_0^{2\pi} d\theta \phi(r, z_i, \theta), \quad (2.13)$$

where $k = \text{min, max, mid}$ indicates the location of interest at $R(z) = R_{\text{min}}, R_{\text{max}}, R_{\text{mid}} = \bar{R}$; N_k is the respective number of cross-sections, and ϕ the target variable, that is, the velocity components and their squares. To enable consistent comparison between different axial regions despite local variations in pipe radius, the radial coordinate is rescaled relative to the maximum radius R_{max} such that the rescaled radial coordinate r' is defined as

$$r' = \frac{r}{R(z)} R_{\text{max}}. \quad (2.14)$$

This transformation maps all radial profiles onto a common reference frame. Furthermore, we display the results in terms of the distance from the wall, which is given by $y = R_{\text{max}} - r'$, and in terms of the distance in wall units, which is $y^+ = yu_\tau/\nu$.

The global average is obtained by averaging the profiles at the same rescaled wall distance as

$$\langle \phi \rangle(y) = \frac{1}{2\pi L_z} \int_0^{L_z} dz \int_0^{2\pi} d\theta \phi[(R_{\text{max}} - y)R(z)/R_{\text{max}}]. \quad (2.15)$$

That is, we average velocities at the same relative distance to the wall. Specifically for strong wall fluctuation, this accounts for the fact that the position of the boundary layer may vary along the wavy wall contour. In the following, we employ for the average streamwise velocity component the notation $U(y) \equiv \langle u_z \rangle$, and in wall units $U^+(y^+) \equiv U(y^+ \nu/u_\tau)/u_\tau$.

Pipes are considered smooth if the roughness height is smaller than the viscous sublayer, $k^+ \ll 1$. For large $Re \gg 1$ an inertial range develops for $y \gg \nu/u_\tau$ in which the only relevant length scale is the distance to the wall. The average velocity profile for $y^+ \gg 1$, is then given by the logarithmic law (Cohen & Kundu 2004)

$$U^+ = \kappa^{-1} \ln(y^+) + A, \quad (2.16)$$

where $\kappa = 0.4$ is the von-Karman constant, $A \approx 5$ is an additive constant that depends on the flow conditions close to the wall. For rough surfaces ($k^+ \gg 1$) flow behaves similarly to smooth surfaces at distances $y \gg k$ large compared to the characteristic roughness length Townsend (1976), and follows (Chung *et al.* 2021)

$$U^+ = \kappa^{-1} \ln(y/k) + B(k^+), \quad (2.17)$$

where B depends on the wall geometry and roughness Reynolds number. In order to identify the log-law from numerical data and compare profiles in the outer layer for different roughness heights, we consider a wall offset ℓ or virtual origin (Raupach *et al.* 1991; Chung *et al.* 2021) such that the origin of $\bar{y} = R_{\text{max}} - r' - \ell$ is located at a distance ℓ from the wall. We define here ℓ as a fraction of the roughness height that is determined by the ratio between the equivalent hydraulic radius and the maximum radius as discussed in Section 3.4. In the following we use the notation \bar{y} when we refer to velocity profiles with respect to the virtual origin.

For rough surfaces, the mean velocity decreases with respect to the one for smooth surfaces at the same or similar Re_τ . This velocity deficit is quantified by the roughness

Case	Symbol	\bar{R}/k	Δr_{min}^+	$\Delta\theta^+$	Δz^+	Re_b	Re_h	Re_τ	T/τ_t	$f \times 10^2$
Smooth pipe	---	[-]	0.032	0.46	0.89	2000	2000	32	63.24	3.2
2k-10	○	10	0.038	0.51	1.03	2000	1886	68.58	77.16	4.23
2k-5	□	5	0.065	0.84	1.80	2000	1687	103.28	72.61	11.99
2k-3.3	△	10/3	0.0897	1.10	2.47	2000	1488	121.03	65.59	21.17
2k-2	◇	2	0.139	1.57	3.83	2000	1112	125.46	60.88	40.73
Smooth pipe	---	[-]	0.093	1.31	2.55	5300	5300	181.4	61.62	3.7
5k-10	○	10	0.123	1.66	3.39	5300	4997	225.13	76.47	6.49
5k-5	□	5	0.191	2.46	5.27	5300	4470	302.62	80.29	14.67
5k-3.3	△	10/3	0.257	3.17	7.09	5300	3943	345.05	70.57	24.5
5k-2	◇	2	0.387	4.39	10.68	5300	2947	354.52	56.26	46.31

Table 1. Flow parameters for flow in wavy pipes. The table is divided in two sets of bulk Reynolds number $Re_b = 2R_{max}u_b/\nu$, respectively 2000 and 5300. \bar{R}/k_s is the inverse relative roughness, comparing the average radius and the wall roughness k . Minimum Δr^+ , $\Delta\theta^+$ and Δz^+ are the grid spacing in the in the cross-stream and streamwise direction, in wall units, for the mesh with $145 \times 113 \times 881$ grid points in the radial, azimuthal and axial direction respectively. The Re_b is the bulk Reynolds number, defined with maximum aperture. The $Re_h = 2R_h u_b/\nu$ is the Reynolds number in terms of the equivalent hydraulic radius defined by Eq. (3.2), $Re_\tau = R_h u_\tau/\nu$ is the friction Reynolds number. T/τ_t is the non-dimensional averaging time expressed in eddy turnover units, where $\tau_t = R/u_\tau$. As last $f = 8\tau_w/(\rho u_b^2)$ is the friction factor.

function ΔU^+ . We write the mean velocity for the wavy pipe as

$$U^+ = \kappa^{-1} \ln(y^+) + A - \Delta U^+, \quad \Delta U^+ = \kappa^{-1} \ln(k^+) + A - B(k^+). \quad (2.18)$$

We use the roughness function ΔU^+ in order to characterize and measure the impact of roughness on the mean flow behavior. For rough pipes, the equivalent sand-grain roughness k_s^+ has been used as a hydrodynamic concept to quantify the impact of wall roughness on flow. It can be defined by inverting the Colebrook relation for the velocity deficit (Jimenez 2004; De Maio *et al.* 2023)

$$\Delta U^+ = \frac{1}{\kappa} \ln(1 + 0.3 k_s^+). \quad (2.19)$$

As stressed by Jimenez (2004), k_s is a hydrodynamic concept that needs to be related to the actual surface geometry to be used as a meaningful roughness descriptor. We will discuss this question in Section 3.5.

2.3. Numerical simulations

The direct numerical flow simulations are performed using the spectral element code Nek5000 (Fischer *et al.* 2008), which numerically integrates the incompressible Navier-Stokes equations (2.5). The pipe length is set to $L_z = 14R_{max}$. This choice follows the recommendation by Wu & Moin (2008), who indicate that the maximum wavelength in pipe flow is between 8 and 16 times the pipe radius.

2.3.1. Mesh

To discretise the geometry, an unstructured hexahedral mesh is employed. The mesh is specifically designed to resolve the near-wall region adequately while maintaining sufficient accuracy in the pipe centre. The grid is uniformly distributed along the streamwise direction. In the radial direction a non-uniform geometric compression is applied to ensure adequate resolution at the wall and to avoid unnecessary cells in the centre of

the tube. The transition is performed in a way to avoid significant skewness. At the pipe centre the cells are approximately cube shaped ($\Delta r \approx \Delta r\theta \approx \Delta z$). Several previous numerical studies have highlighted the importance of adequately resolving flow near rough or modulated walls (Busse *et al.* 2015; Chan *et al.* 2015; De Maio *et al.* 2023), typically recommending a minimum of 12–15 grid points per roughness element. Although the present geometry involves smooth, large-scale periodic modulation rather than small-scale roughness, the adopted mesh provides 24–60 radial grid points, depending on the roughness amplitude. This ensures sufficient resolution of near-wall gradients and recirculation features, particularly as larger-amplitude cases occupy a greater portion of the radial domain. The numerical setup for the different pipe geometries under consideration are given in Table 1 for the bulk Reynolds numbers $Re_b = 2000$ and 5300.

2.3.2. Time step and averaging time

All simulations are performed with a Courant-Friedrichs-Lewy (CFL) number maintained below unity to ensure numerical stability. The timestep, expressed in wall units as $\Delta t^+ = u_\tau^2 \Delta t / \nu$, ranges from 0.16 to 0.489. After the initial transient, each case is continued for a statistically converged averaging period, summarised in Table 1. The total averaging time, non-dimensionalised as $T/\tau_t = Tu_\tau/R_{\max}$, spans between approximately 56 and 80 eddy turnover times, depending on the configuration. This corresponds to about 10–32 bulk flow-through times, based on Tu_b/L_z . These averaging intervals are consistent with those employed in recent high-fidelity simulations (Chan *et al.* 2015; Pirozzoli *et al.* 2021; De Maio *et al.* 2023) and were found here to provide reliable convergence of first-order statistics and satisfactory convergence of second-order moments for the aims of this study.

2.3.3. Flow initialisation and laminar-turbulent transition

For the smooth-wall pipe, the flow is initialised with a parabolic velocity profile and small-amplitude random perturbations added to promote transition. At low bulk Reynolds numbers, particularly in the transitional regime ($Re_b = 2500$ – 4000), these perturbations are subject to viscous dissipation and may decay, potentially leading to relaminarisation. To prevent this, the viscosity is temporarily reduced, equivalent to imposing a higher Reynolds number, which allows the perturbations to grow and initiate the transition to turbulence. An initial stabilisation phase of approximately 5000 timesteps is used to ensure numerical stability.

For the wavy-wall pipes, the flow perturbation due to the large-amplitude roughness naturally drives the laminar-turbulent transition. However, to accelerate the development of a statistically steady turbulent state, the initial velocity field is obtained by interpolating from a fully developed smooth-wall case. A similar stabilisation strategy is adopted, with a longer initial phase of around 20,000 timesteps used before time averaging is initiated.

2.3.4. Validation

The numerical set-up was first validated by simulating turbulent flow in a smooth circular pipe at a bulk Reynolds number $Re_b = 5300$. The computed wall shear stress was $\tau_w = 4.6875 \times 10^{-3}$, corresponding to a friction Reynolds number $Re_\tau = u_\tau R/\nu \approx 180$, within 1% of the canonical value (Wu & Moin 2008). For this reference case, the near-wall mesh resolution was $\Delta r_{\min}^+ \approx 0.09$, while the wall-parallel spacings were $\Delta\theta^+ = 1.13$ in the azimuthal direction and $\Delta z^+ = 2.55$ in the streamwise direction. The mesh was not tailored to this smooth configuration, but rather designed a priori to satisfy resolution requirements under the most demanding conditions of the study, namely the wavy pipe with the largest geometric amplitude and highest Reynolds number. Furthermore, the wall-unit spacings across all rough cases remain within DNS standards, including $\Delta r^+ \lesssim 1$,

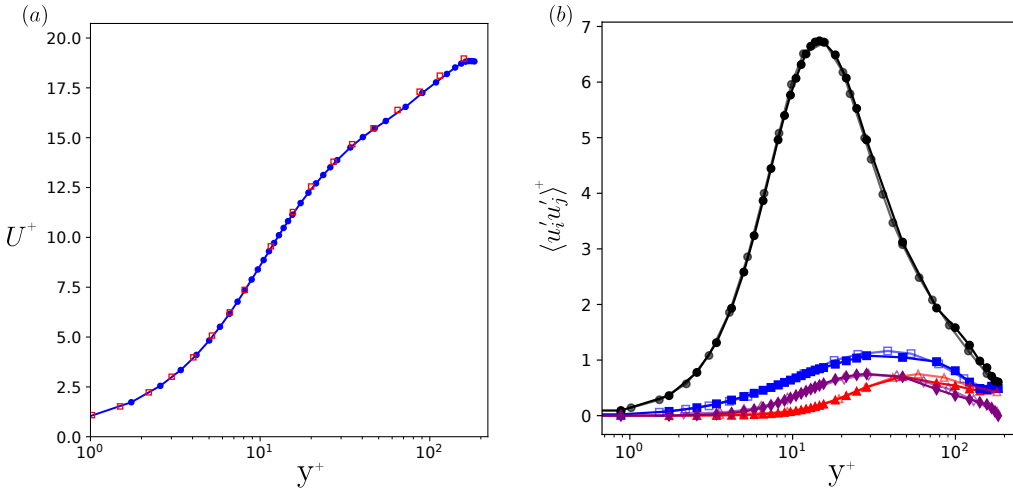


Figure 2. (a) Mean velocity profile in wall units (U^+ vs. y^+), comparing the present simulation with the reference data of Pirozzoli *et al.* (2021), shown as empty squares. The viscous sublayer and logarithmic region are included as a validation benchmark for the numerical framework at $Re_\tau = 180$. (b) Reynolds stress components normalised by the friction velocity squared (u_τ^2) as functions of y^+ . Shown are the velocity variances $\langle u_r'^2 \rangle^+$ (Δ), $\langle u_\theta'^2 \rangle^+$ (\square), $\langle u_z'^2 \rangle^+$ (\circ), and the Reynolds shear stress $\langle u_r' u_r' \rangle^+$ (\diamond). Filled markers denote the present simulation, and empty markers indicate the reference data.

$\Delta\theta^+ \lesssim 6$, and $\Delta z^+ \lesssim 15$, even under the most severe flow conditions as suggested for smooth-wall flows (Piomelli 1993; Moser *et al.* 1999). Full resolution statistics for every case are listed in Table 1. Figure 2 compares the present results for mean and second-order statistics with those of Pirozzoli *et al.* (2021), showing very good agreement. Figure 2(a) presents the rescaled streamwise velocity profile, with the mean velocity expressed in wall units as $U^+ = u/u_\tau$ and the wall-normal coordinate as $y^+ = yu_\tau/\nu$. Figure 2(b) shows the turbulence statistics, including the velocity variances $\langle u_r'^2 \rangle^+$, $\langle u_\theta'^2 \rangle^+$, $\langle u_z'^2 \rangle^+$, and the Reynolds shear stress $\langle u_r' u_r' \rangle^+$.

3. Results

The results are structured in three parts to progressively build the analysis and highlight the effects of both surface roughness and flow inertia. The first section focuses on a single reference case ($Re_b = 2000$, $k = 0.2$) and serves to introduce the analysis framework. Here, the data processing approach is explained, and the key flow features induced by surface waviness, such as local acceleration, separation, and wall-shear variation, are examined in detail. This sets the foundation for interpreting more complex cases. In the second part, the effect of roughness height is investigated systematically while keeping the Reynolds number fixed. This allows for isolating the influence of geometric forcing on the internal flow dynamics and the emergence of localised transitional behaviours. Finally, the combined influence of Reynolds number and surface roughness is considered. Rather than isolating inertia alone, this section explores how increasing flow rates interact with different levels of roughness, providing a more complete picture of how both parameters shape the flow regime, from laminar through transitional and into turbulence.

3.1. Deviations from classical laminar flow due to wall waviness

To illustrate the main flow features introduced by surface waviness, the case at bulk Reynolds number $Re_b = 2000$ and roughness amplitude $\bar{R}/k = 2$ is selected as a reference.

Although this Reynolds number typically lies within the laminar regime for a smooth pipe, geometric forcing induces complex dynamics that deviate from classical behaviour (Nishimura *et al.* 1984; Smith 1986). In smooth pipes, the Reynolds number is usually defined using a constant diameter D , assuming uniform cross-section and fully developed conditions. In the present geometry, the sinusoidally varying radius leads to local velocity changes and pressure gradients, making a global Reynolds number inadequate. A local Reynolds number can be defined from the geometry as $Re_{loc}(z) = u_b D(z)/\nu$, which better captures local flow variations, particularly in regions of strong expansion or contraction. Figure 3(a) shows the variation of $Re_{loc}(z)$ over one wavelength for different roughness levels. At the highest roughness, the local Reynolds number fluctuates by over 800 units, indicating the possible coexistence of laminar, transitional, or even turbulent regimes within a single wavelength.

Figure 3(b) shows isolines of the streamwise velocity field extracted from a vertical mid-plane of the pipe ($x = 0$), covering one wavelength between two consecutive contractions. As the flow enters the narrowing section, isolines are compressed toward the wall due to local acceleration. In the subsequent expansion, a recirculation region develops near the lower wall, marked by reversed flow. The uneven spacing and curvature of the isolines indicate the presence of secondary motions, suggesting that the interaction between geometry and inertia induces local instabilities. These instabilities are periodically regenerated by the repeating constrictions, promoting complex flow patterns even at moderate global Reynolds numbers.

Figure 4(a) shows the dimensionless velocity profiles (U^+ vs y^+) for three characteristic cross-sections within the wavy pipe: at minimum radius (R_{min}), midpoint radius (R_{mid}), and maximum radius (R_{max}). The profiles reveal significant deviations from the canonical smooth pipe profile, primarily due to the interaction between the wavy geometry and the flow. At R_{min} , the velocity is elevated due to local acceleration through the narrow section, yet the dimensionless velocity remains low because the wall shear stress increases proportionally. In contrast, the R_{max} profile exhibits a reversed flow near the wall, indicating a recirculation bubble driven by an adverse pressure gradient in the expansion zone. This is consistent with the isolines shown in Fig. 3(b), where flow separation occurs. The midpoint profile (R_{mid}) shown here represents an average of the two midpoints within

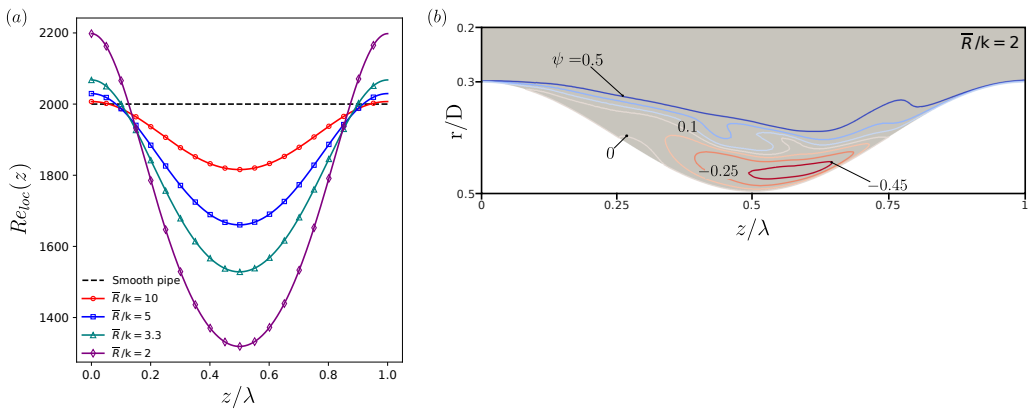


Figure 3. Flow features in a wavy pipe with roughness height $\bar{R}/k = 2$ at bulk Reynolds number $Re_b = 2000$. (a) Streamwise distribution of the local Reynolds number $Re_{loc}(z)$, calculated using the local axial velocity and pipe cross-sectional area, over one wavelength. (b) Time averaged isolines contours of the main component of the velocity field in the lower half of the pipe cross-section, highlighting flow separation and recirculation near the diverging region of the wavy wall.

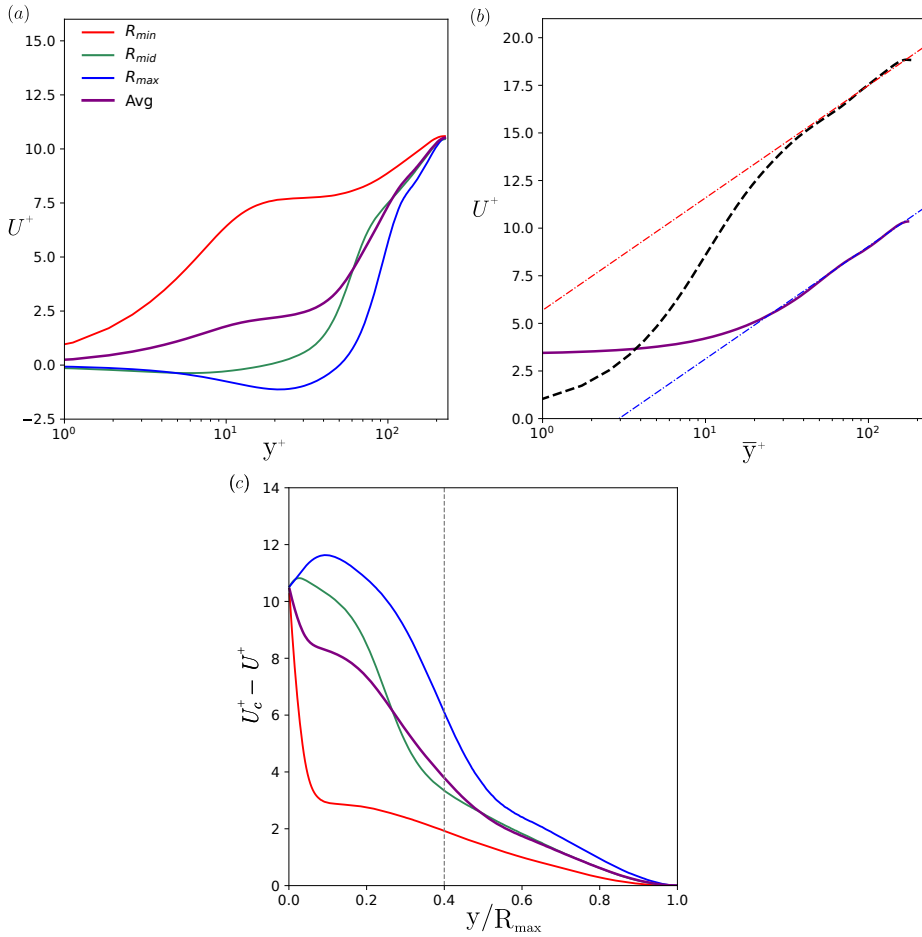


Figure 4. Inner-scaled flow statistics in a wavy pipe with roughness height $\bar{R}/k = 2$ and bulk Reynolds number $Re_b = 2000$. (a) Mean streamwise velocity profiles U^+ as a function of wall-normal distance y^+ . Profiles are shown at three characteristic cross-sections: minimum radius R_{min} , mid-wave R_{mid} , and maximum radius R_{max} . The Avg curve represents the spatial average of the velocity profile along the entire pipe. (b) Evaluation of the roughness function ΔU^+ . The mean streamwise velocity profiles for the case is compared with smooth pipe at comparable Re_τ resulting in a $\Delta U^+ = 8.22$. (c) Velocity defect profiles $U_c^+ - U^+$, plotted against the outer-scaled coordinate y/R_{max} . The vertical dashed line positioned at $y/R_{max} = 0.4$, correspond to the location of the crest for the current geometry. Colours are consistent across all panels.

a wavelength, one located before the divergence and one after. As the flow approaches the expansion, the midpoint profile shows signs of detachment (negative values), while after the expansion, it shows reattachment. Consequently, the averaged profile shown here masks these contrasting behaviours, giving an intermediate representation. The profile obtained from averaging in the streamwise direction offers a comprehensive view of the overall flow behaviour. However, this averaging process inevitably smooths out localised effects, masking the distinct features associated with individual cross-sections. The results indicate that the large amplitude of the wavy pipe significantly modifies the near-wall flow dynamics, promoting localised flow separation and complex secondary motions even at a Reynolds number typically associated with laminar conditions. When compared to a smooth pipe, the velocity profiles suggest a clear departure from laminar behaviour. For instance the Re_τ and looking at the friction factor profile in Fig. 10, the case lies well

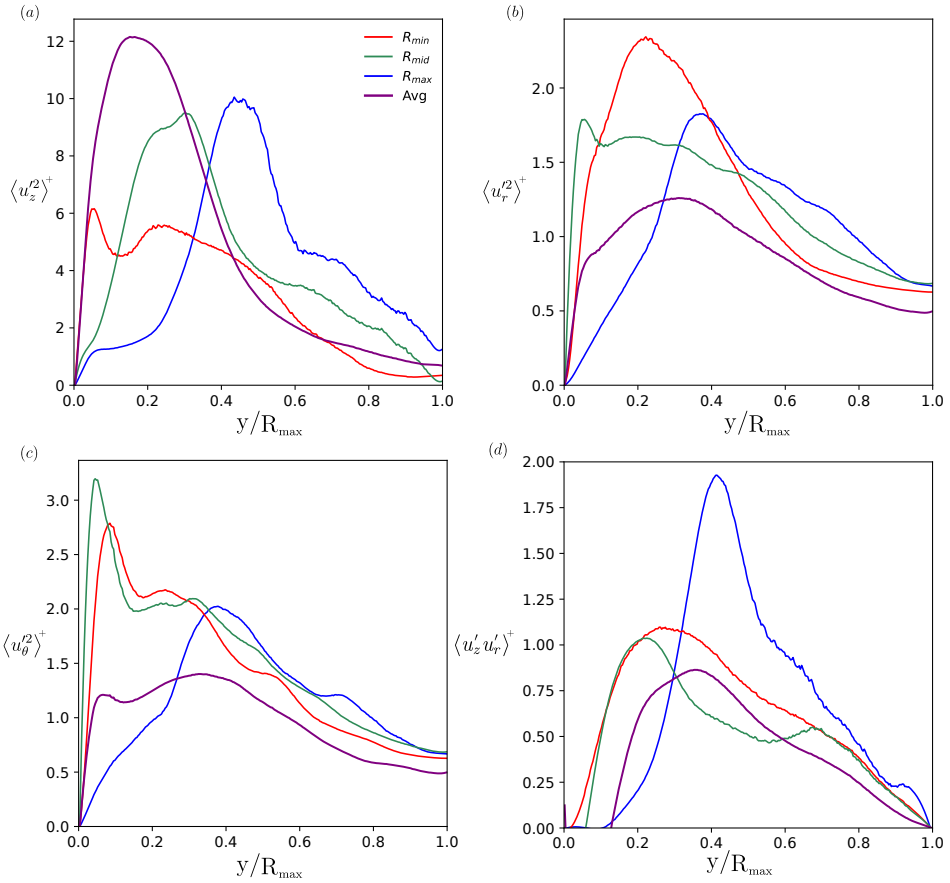


Figure 5. (a) Axial $\langle u_z'^2 \rangle^+$, (b) radial $\langle u_r'^2 \rangle^+$, (c) azimuthal velocity variances $\langle u_\theta'^2 \rangle^+$, (d) Reynolds stresses $\langle u_r' u_z' \rangle^+$ with matching styles for the three cross-sections and the axial-average.

above the laminar prediction. The flow field exhibits characteristics consistent with weak turbulence or transitional flow, despite being nominally in the laminar regime based on the bulk Reynolds number. This is typical of rough pipes with strong geometric forcing, where early transition is driven by flow instabilities induced by the wall topography. Further insight is obtained by examining the roughness function ΔU^+ , Fig. 4(b), defined as the difference between the inner-scaled mean velocity profile and that of a smooth pipe at comparable Re_τ . The results show a marked velocity deficit $\Delta U^+ \approx 8$, indicating significant deceleration in the near-wall region due to the enhanced frictional resistance. A similar trend was observed in the DNS study of Saha *et al.* (2015), where the wavy geometry led to flattened mean profiles and extended logarithmic layers, despite modest Reynolds numbers. While the exact shape of the velocity profiles differs due to variations in geometry and Reynolds number, the qualitative resemblance supports the conclusion that the imposed wall waviness triggers early transition and sustained turbulent-like behaviour.

Panel (c) shows the inner-normalised velocity defect, defined as $U_c^+ - U^+$ where U_c^+ is the centreline velocity at each section. In the contraction, the defect decreases steeply from the wall, indicating a more plug-like velocity profile forced by rapid axial acceleration. At the expansion, the defect is larger near the wall and shows a flatter growth, consistent with the presence of recirculation and reduced near-wall shear. The midpoint profile falls

between these two extremes, and the streamwise-averaged defect retains a non-canonical shape, further confirming the influence of geometric modulation.

Figure 5 presents the velocity variances and Reynolds shear stresses at three streamwise locations, together with their streamwise-averaged profiles. The results show that the wavy geometry modulates turbulence not only in amplitude but also in its spatial organisation and anisotropy.

The axial variance, $\langle u_z'^2 \rangle$, displays the strongest dependence on geometry. At the constriction (R_{\min}), a secondary near-wall peak indicates that production occurs in two distinct regions: within the wall layer and in an outer shear layer generated by local acceleration. Toward the expansion (R_{\max}), this outer contribution dominates and shifts away from the wall, consistent with a region of deceleration and flow separation where the shear layer replaces the logarithmic region as the main production site. The streamwise-averaged profile therefore exceeds the local ones, not through simple averaging, but because zones of strong production, particularly near R_{\max} , contribute disproportionately to the total turbulent kinetic energy. The radial variance, $\langle u_r'^2 \rangle$, increases moderately and its peak moves outward with expansion, reflecting enhanced wall-normal motions in separated or strongly decelerated regions. However, the streamwise average remains smaller than the local maxima, as these wall-normal events are intermittent and spatially confined. Unlike canonical pipe flow, the maximum $\langle u_r'^2 \rangle$ occurs farther from the wall, indicating that large-scale motions dominate turbulent transport rather than near-wall streaks.

The azimuthal variance, $\langle u_\theta'^2 \rangle$, decreases from R_{\min} to R_{\max} , suggesting that curvature-induced secondary motions redistribute energy toward the axial and radial components in the expansion. A weak double peak appears at R_{\min} , likely associated with local three-dimensional strain and secondary vortices rather than classical outer-layer dynamics. The Reynolds shear stress, $\langle u_r' u_z' \rangle$ (d), departs markedly from the near-linear trend $\langle u_r' u_z' \rangle^+ \sim \tau_w(1 - r/R)$ typical of smooth pipes. Its outward shift and amplification at R_{\max} indicate that momentum transfer is dominated by outer-layer eddies generated by adverse pressure gradients, while at R_{\min} the stress is confined to the near-wall region. Scaling the profiles with a global friction velocity accentuates these differences, reflecting significant streamwise variations in local wall stress.

Overall, the results show that the wavy geometry alters the spatial organisation and relative importance of turbulent motions, shifting production away from the wall and modifying the balance between velocity components. These effects arise already at moderate Reynolds number, showing that curvature and pressure-gradient forcing can profoundly reshape turbulent structure well before the fully rough regime is reached. It should be noted that the local profiles are obtained from a limited number of cross-sections and may therefore be influenced by spatially localised flow features. In contrast, the streamwise-averaged profiles integrate over a much larger sample, smoothing out fluctuations and spatial intermittency. This discrepancy may explain part of the apparent amplification observed in the averaged profiles. To assess these trends more systematically and improve statistical convergence, simulations over a longer pipe domain would be required.

3.2. Flow response to increasing wall roughness

To systematically assess the effect of surface waviness on internal flow structure, we fix the bulk Reynolds number at $Re_b = 2000$, the same value used in the previous section. This choice is deliberate: at this Reynolds number, flow in a smooth pipe remains fully laminar, offering a clean baseline from which to evaluate the impact of geometric perturbations. By holding inertia constant and varying only the roughness amplitude, from $\bar{R}/k_s = 10$ to 2, we

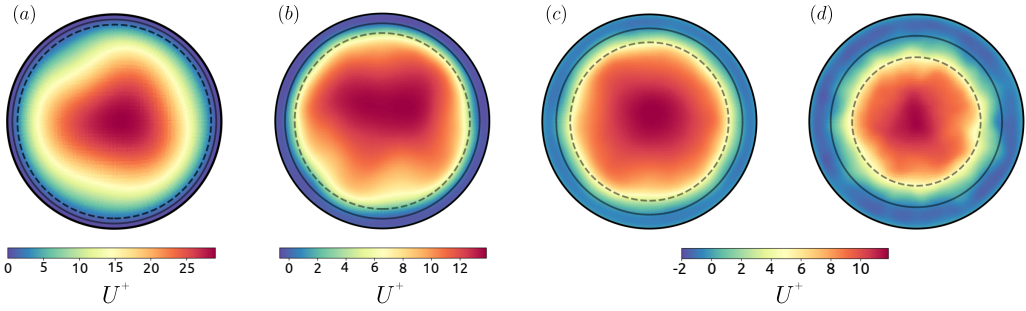


Figure 6. Contours of mean streamwise velocity for the different roughness level for the case $Re_b = 2000$ extracted at the correspondence of the divergence $R = R_{\max}$. The solid line represents the mean radius (\bar{R}) and the dashed line depicts the plane of the peak of the roughness ($R = R_{\min}$).

ensure that any observed changes in flow behaviour arise solely from increased geometric forcing. This isolates the contribution of surface roughness to flow destabilisation, allowing us to identify the onset of recirculation, deviations from classical wall-scaling, and the emergence of localised transitional features induced purely by geometry.

Figure 6 presents contours of the mean streamwise velocity U^+ , extracted at the axial location corresponding to the maximum cross-sectional area, for increasing levels of surface roughness. In panel (a), corresponding to the smallest roughness amplitude $\bar{R}/k = 10$, the flow preserves a near-parabolic profile, although slight deviations from symmetry are already visible. As roughness increases from panels (b) through (d), the velocity distribution becomes progressively flatter and more distorted. A significant drop in core velocity appears, accompanied by steeper gradients near the wall. Indications of recirculation appear in panel (b), although they remain weak and confined to narrow regions. In panel (c), these zones become more prominent, with distinct regions of reversed flow visible particularly in the region between the mean and maximum radius. By panel (d), recirculation is clearly established and occupies a substantial portion of the near-wall region. The solid and dashed circles in each plot mark the mean radius \bar{R} and the minimum radius R_{\min} , respectively, helping to visualise the relative displacement of high- and low-velocity regions within the perturbed geometry. As roughness increases, the near-wall region becomes dominated by reverse and low-speed flow, forming a multilayered structure that departs from classical wall scaling. This structure consists of a reversed near-wall zone, a velocity-deficit region, and a high-shear interface with the bulk flow.

Figure 7 provides a wall-normal perspective on how the mean flow and fluctuation structure evolve with increasing roughness. Panel (a) compares the dimensionless mean streamwise velocity profiles U^+ , both streamwise-averaged and extracted at the maximum radius cross-section. For the smallest roughness level ($\bar{R}/k_s = 10$), the average profile is nearly indistinguishable from the smooth-pipe reference, suggesting that the overall drag remains comparable and the geometric forcing is minimal. The only visible deviation appears locally at R_{\max} , where streamlines bend to accommodate the pipe curvature, but no significant velocity deficit is observed, as no flow reversal is identified. In contrast, at $\bar{R}/k_s = 5$, the curvature becomes strong enough to generate local flow reversal in the expansion region, leading to negative velocities near the wall. As roughness increases further, the R_{\max} and streamwise-averaged profiles increasingly diverge. Interestingly, the near-wall local behaviour up to $y^+ \approx 6$ remains nearly identical across all cases. Beyond this point, the profiles within the recirculation zones begin to separate and shift towards the pipe centre. Once the flow exits the separated region and re-accelerates, the profiles appear

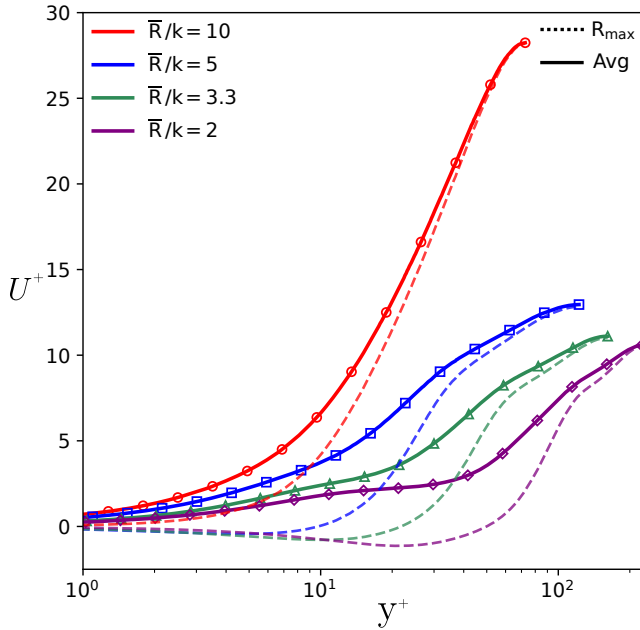


Figure 7. Inner-scaled mean velocity profiles U^+ versus wall-normal distance y^+ in wavy pipes with varying roughness configurations at $Re_b = 2000$. Dotted lines denote profiles extracted at the cross-section of maximum pipe radius R_{\max} (divergent region), while solid lines represent streamwise-averaged profiles.

to follow a similar trend again. For the averaged profiles, the near-wall slope becomes flatter with increasing roughness, reflecting stronger drag effects. Another noteworthy observation is that the profiles for $\bar{R}/k_s = 3.3$ and 2 collapse in the core region, reaching nearly the same maximum U^+ . This suggests that further increases in roughness do not lead to stronger deceleration of the core flow, possibly indicating a saturation of the geometric effect on the centreline velocity. The flow appears to have entered a regime where the increased drag and recirculation suppress any additional deformation of the mean profile (Jimenez 2004).

Figure 8 shows the streamwise-averaged velocity variances and Reynolds shear stresses for different roughness heights, presented in outer scaling with y/R_{\max} as the wall-normal coordinate. The axial variance, shown in panel (a), exhibits peaks that remain close to the wall for all cases, indicating that most of the turbulent energy is confined to the near-wall region even at higher roughness. The profiles show little variation outside the region influenced by the pipe divergence, and a similar trend is observed for the smooth-pipe reference. Likewise, the radial and azimuthal variances collapse beyond the wavy sublayer, suggesting that outer-layer dynamics remain largely unaffected by the surface modulation.

The radial variance, panel (b), increases in magnitude with roughness and shows a mild outward displacement of its maximum. This behaviour reflects the strengthening of wall-normal motions and the enhanced cross-stream transport associated with the geometric modulation. The azimuthal variance, panel (c), also grows with roughness, developing a broader outer shoulder for the roughest cases. This indicates a redistribution of energy from the axial to the azimuthal direction, likely driven by curvature and secondary motions that become more prominent with surface waviness.

The Reynolds shear stress profiles, panel (d), show that over a considerable portion of the outer region, the curves collapse onto the expected linear smooth-wall behaviour. This

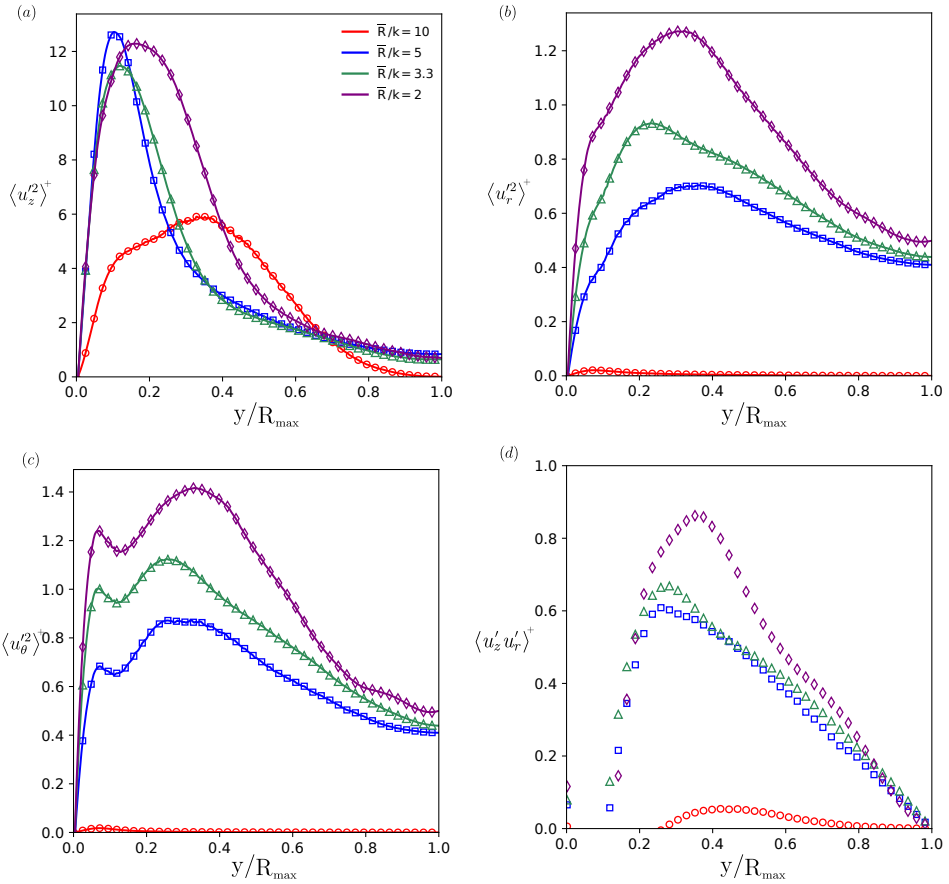


Figure 8. Axial averages of the variances of the (a) axial ($\langle u_z'^2 \rangle^+$), (b) radial ($\langle u_r'^2 \rangle^+$), and (c) azimuthal ($\langle u_\theta'^2 \rangle^+$) velocities for different roughness heights at $Re_b = 2000$. Panel (d) shows the corresponding Reynolds shear stress ($\langle u_z' u_r' \rangle^+$). Results are presented in outer scaling, with y/R_{\max} as the wall-normal coordinate.

suggests that despite the geometric modulation near the wall, the large-scale momentum transfer in the outer region follows a similar scaling to that of smooth-pipe turbulence.

3.3. Interplay between flow inertia and surface roughness

In this last section both effects of Reynolds number and roughness are considered. Figure 9 presents time-averaged streamline contours of the streamwise velocity field in the lower half of the pipe cross-section, highlighting the development of separation zones near the diverging regions of the wavy wall. The panels are arranged with increasing roughness amplitude from top to bottom (i.e., decreasing \bar{R}/k), and increasing bulk Reynolds number Re_b from left to right. For each configuration, the first appearance of a recirculation bubble is outlined in red, providing an upper bound on the separation threshold. It is important to note that this does not represent a sharp transition; recirculation may occur at lower Re_b values between those tested, but no finer resolution was explored in this study. For the smoothest configuration ($\bar{R}/k = 10$), the flow remains largely symmetric and attached even up to $Re_b = 1000$, indicating that viscous diffusion dominates and that mild curvature is insufficient to cause separation.

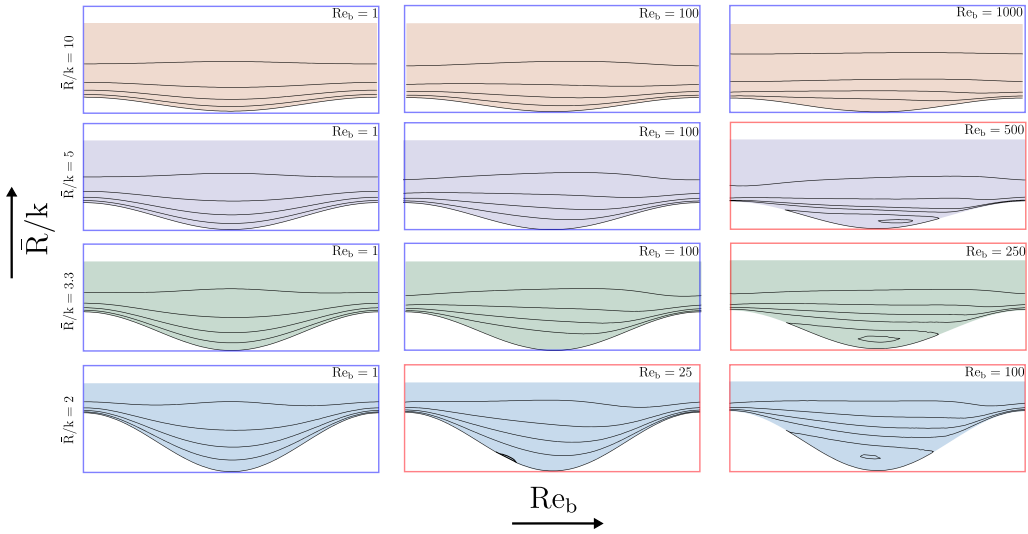


Figure 9. Time-averaged isolines of the main component of the velocity field in the lower half of the pipe cross-section, highlighting flow separation and recirculation near the diverging region of the wavy wall. A set of 3 cases for different relative Reynolds numbers are reported for each pipe configuration. Reynolds values were selected non-uniformly to highlight the earliest Reynolds number at which recirculation first appears in each case.

At intermediate waviness ($\bar{R}/k = 5$ and 3.3) the velocity field becomes progressively distorted as inertia grows. Recirculation first appears at $Re_b = 500$ for $\bar{R}/k = 5$ and at $Re_b = 250$ for $\bar{R}/k = 3.3$. These cases illustrate how even moderate curvature can couple with the nonlinear convective terms to trigger flow reversal once the local inertial forces are strong enough. The roughest configuration ($\bar{R}/k = 2$) shows the earliest onset of separation: no bubble is present at $Re_b = 1$, but a small, steady vortex forms at $Re_b = 25$ and expands markedly by $Re_b = 100$. Strong waviness therefore lowers the critical Reynolds number to the point that separation occurs while the bulk flow is still in a nominally laminar regime. These results suggest that at high waviness, geometry alone can trigger separation, even in the nominally laminar regime. A similar behaviour was reported in the 2D experimental study by Nishimura *et al.* (1984), and further investigated numerically by Wang & Vanka (1995), who adopted the same geometry. Their setup consisted of two sinusoidal plates with a wavelength of $\lambda = 2.8$ units and a peak-to-peak amplitude of $H = 0.7$ units, resulting in an estimated $\bar{R}/k \approx 0.93$. In this configuration, flow remained symmetric and attached at low Reynolds numbers, but recirculation zones first appeared at $Re \approx 15\text{--}20$. Similarly Al-Daamee & Hamza (2024) observed development of secondary flow in the diverging section of the channel at even lower Reynolds numbers $Re \approx 5$. While their geometry is considerably rougher and strictly two-dimensional, the early emergence of separation supports the qualitative trend observed in the pipe flow investigated in this study in particular for the roughest configuration: increasing waviness promotes flow reversal even at relatively low Reynolds numbers. The relative position and extent of these regions shift not only with Re_b but also with \bar{R}/k , implying that the geometry imposes a spatial preference for instability. In all cases where recirculation occurs, reversed flow initiates near the lower wall at the downstream side of the constriction (i.e., in the expanding region of the wave). As \bar{R}/k decreases, this separation point appears earlier along the streamwise coordinate and the recirculation zone expands upstream, indicating

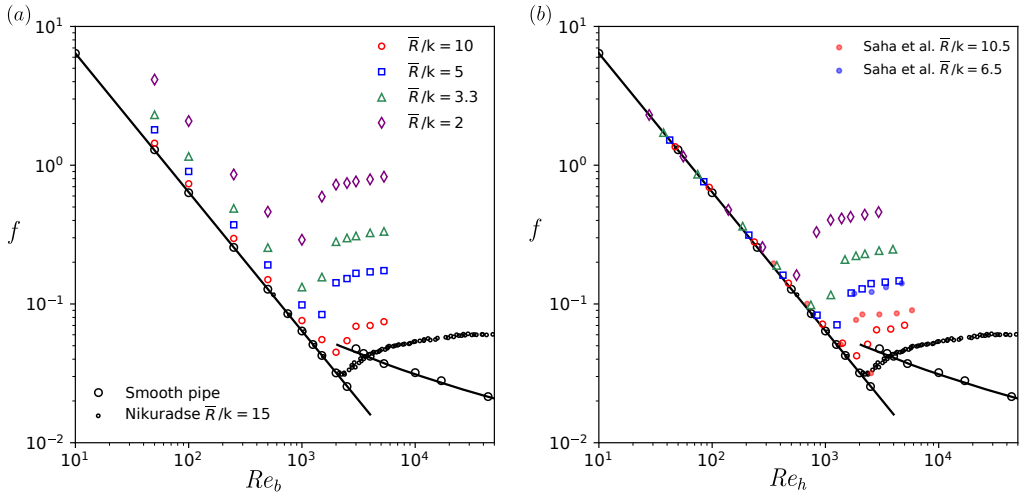


Figure 10. (a) Friction factor (f) versus bulk Reynolds number (Re_b), evaluated with the maximum radius (R_{\max}). (b) Variation of friction factor with the effective bulk Reynolds number (Re_h), based on the effective radius (R_h) evaluated from the laminar simulations ($R_h = \sqrt{8\mu u_b/G}$) and the Prandtl friction laws for laminar and turbulent flow. As a reference, results for the smooth pipe are reported together with the data of Nikuradse (1933) for $\bar{R}/k = 15$, and the results of the investigation by Saha *et al.* (2015) for the geometries with $\bar{R}/k = 10.5$ and 6.5 .

that increased roughness shifts the instability closer to the throat. At larger Reynolds numbers, the vortex grows further, its centre shifts downstream.

This has direct implications for the observed pressure losses. The presence of reversed flow increases local shear and introduces additional energy dissipation through recirculation and reattachment dynamics, even when the flow remains nominally laminar. These structural changes in the flow field, particularly the emergence of recirculation zones well below the turbulent threshold, contribute to the increased friction factors observed in wavy pipes and discussed in the next section.

3.4. Darcy friction factor

Fig. 10 shows the friction factors from the present simulations together with the smooth-pipe prediction and Nikuradse's classical (Nikuradse 1933) data for the highest available relative roughness ($\bar{R}/k_s = 15$). In the laminar regime ($Re_b \leq 2000$), Nikuradse's data collapse onto the theoretical Hagen-Poiseuille prediction, $f = 64/Re_b$, regardless of the roughness level, which implies that geometric roughness does not alter significantly the laminar friction in those experiments. By contrast, our numerically obtained laminar friction factors exceed the theoretical value by 5–80%. Two effects explain the discrepancy. First, using the maximum radius R_{\max} to define the Reynolds number $Re_b = u_b R_{\max}/\nu$ is inadequate, as it overestimates the effective cross-sectional area available to the flow. Second, and more fundamentally, even when the mean radius is adopted, the large relative roughness of the wavy geometry distorts the cross-section sufficiently to reduce the flow-conducting area and raise the measured resistance. Classical theory assumes a fixed pipe radius or diameter, but in rough or corrugated geometries this assumption becomes ambiguous. An alternative geometric definition is the harmonic mean radius, defined over

one wavelength λ defined as follows

$$\langle R \rangle_{harm} = \left(\frac{1}{\lambda} \int_0^\lambda \frac{1}{R(z)} dz \right)^{-1}. \quad (3.1)$$

Unlike the arithmetic mean, the harmonic mean gives greater weight to the narrowest sections of the geometry, which tend to dominate viscous dissipation in laminar flow. This weighting makes it particularly suitable for periodically corrugated geometries such as the present wavy pipe, where constrictions strongly influence hydraulic resistance. The harmonic mean radius can be interpreted as an effective scale that reflects the minimum-constriction control of the flow rate. In this sense, it acts as a one-dimensional geometric simplification of the full three-dimensional geometry, compressing axial variations into a single representative radius. To assess its effectiveness, we defined the Reynolds number using $\langle R \rangle_{harm}$ and compared the resulting friction factors to the theoretical prediction (not shown). The agreement is excellent for weak corrugations ($\bar{R}/k \gtrsim 5$) where the harmonic mean reduces the error to below 10%. However, for stronger waviness, the friction factors systematically exceed the theoretical value, by nearly 40% at $\bar{R}/k = 2$, indicating that geometric constriction alone cannot explain the observed resistance.

For comparison, the effect of defining the Reynolds number using the minimum pipe radius, R_{min} , has also been tested. This choice improves agreement with the theoretical friction factor at all levels of waviness due to its conservative bias, but does so inconsistently. At low roughness levels, it overestimates the resistance; at higher roughness, it begins to underestimate it, although the error remains within $\pm 8\%$. By contrast, the harmonic mean radius provides a more balanced correction, reducing error across all tested cases while retaining a clearer physical interpretation.

A related geometric approach was proposed by De Maio *et al.* (2023), who introduced the hydraulic radius $R_H = 2S/V$, based on the fluid volume V and the wetted surface area S . This metric captures the average cross-sectional efficiency of the conduit and also restores excellent agreement with the Hagen-Poiseuille law for mild corrugations ($\bar{R}/k \gtrsim 5$). However, like the harmonic mean, De Maio's correction fails at higher roughness, where recirculation and secondary flows emerge. These flow features distort the velocity profile and increase resistance in ways that purely geometric metrics, regardless of formulation, cannot capture.

To account for these residual effects, we introduce an effective hydraulic radius R_h obtained from the laminar simulations. It is defined in the spirit of an effective conductance as the radius of an equivalent straight pipe that has the same laminar flow resistance as the wavy pipe. The Hagen-Poiseuille law thus gives

$$R_h = \sqrt{\frac{8\mu u_b}{G}}. \quad (3.2)$$

We define the effective hydraulic Reynolds number and friction factor in terms of R_h as

$$Re_h = \frac{2R_h u_b}{\nu}, \quad f_h = \frac{4R_h G}{\rho u_b^2}. \quad (3.3)$$

With these definitions, the laminar data of the friction factor aligns with $f = 64/Re_h$, and therefore embeds the influence of the distorted wall shape in the length scale itself. As shown in Figure 10(b) this rescaling successfully collapses the laminar friction factor data onto the theoretical line, using the adjusted Reynolds number Re_h . For comparison, De Maio *et al.* (2023) also examined laminar flow in rough pipes with high relative

roughness ($\bar{R}/k_s \approx 5$) and reported friction losses approximately 15% lower than those observed in our simulations. The discrepancy likely reflects differences in the nature of the wall geometry: their roughness is randomly textured, whereas our configuration is smoothly but periodically wavy. While both share similar amplitude-to-radius ratios, the spatial organisation of the roughness appears to be a significant factor in determining laminar-flow resistance. The figure also includes the direct-numerical-simulation results of Saha *et al.* (2015), for two comparable roughness levels ($\bar{R}/k = 10.5$ and 6.5), which display the same qualitative behaviour. However, some quantitative differences remain, likely due to their use of a purely geometric correction based on the hydraulic diameter ($D_h = 4A/P$), whereas our approach incorporates a flow-informed adjustment to better capture the impact of recirculation and distortion in the laminar regime.

3.5. Equivalent sand-grain roughness

As discussed previously, the traditional use of effective geometric diameters may underpredict the pressure loss in rough pipes, especially in regimes where flow separation begins but turbulence has not yet fully developed. This stresses the limitations of empirical models that rely solely on geometric corrections to predict pressure losses in rough or undulating conduits. The effective hydraulic radius R_h is a hydrodynamic concept that relates flow rate and pressure drop in the laminar regime. In the same vein, the equivalent sand-grain roughness is a hydrodynamic concept introduced by Jimenez (2004) that characterizes the flow in the fully rough regime. In Figure 11(a), the mean streamwise velocity profiles U^+ are shown for the different roughness levels and Reynolds numbers. The profiles are plotted against the inner-scaled wall-normal coordinate \bar{y}^+ , adjusted to account for the virtual origin associated with each pipe configuration. Increasing roughness (decreasing \bar{R}/k) leads to a progressive downward shift of the profiles in inner units, consistent across the range of Reynolds numbers considered. For clarity, only for the highest Reynolds number case, a dashed line is included for each configuration to indicate the functional relation $U^+ = (1/\kappa) \log(\bar{y}^+) + A$. This serves to highlight the region where the logarithmic behaviour is established and to enable comparison with the smooth pipe profile at a comparable friction Reynolds number Re_τ . A consistent feature observed in the mean velocity profiles is the weak sensitivity of U^+ to the Reynolds number within the range investigated, particularly at higher roughness levels. While some deviations are visible in the outer region for the smoother configurations, the overall collapse of the profiles at different Re_b indicates that turbulence dynamics are primarily governed by the wall geometry once roughness effects become significant. This behaviour is consistent with the transition towards the fully rough regime described by Jimenez (2004), where the flow becomes largely independent of viscous scaling and dominated by pressure drag induced by the surface roughness.

The systematic downward shift of the profiles with increasing roughness intensity shown in panel (a) further supports this interpretation as also observed by Saha *et al.* (2015). In their study, the mean velocity profiles were obtained only up to the minimum wall radius R_{\min} . This implies that the averaging excludes the crest regions of the corrugation, effectively shifting the virtual origin of the wall inward. As a result, their profiles do not extend to $y^+ \lesssim 3$, limiting insight into the immediate near-wall behaviour. In contrast, our simulations retain the full wall-normal extent, resolving the velocity profile all the way to the local wall, including crest regions. This allows a more complete characterisation of the roughness-induced deceleration in the viscous sublayer and the roughness function ΔU^+ . In Appendix 3.5, the results are presented with the same procedure of Saha *et al.* (2015) for the extraction of the averaged profiles.

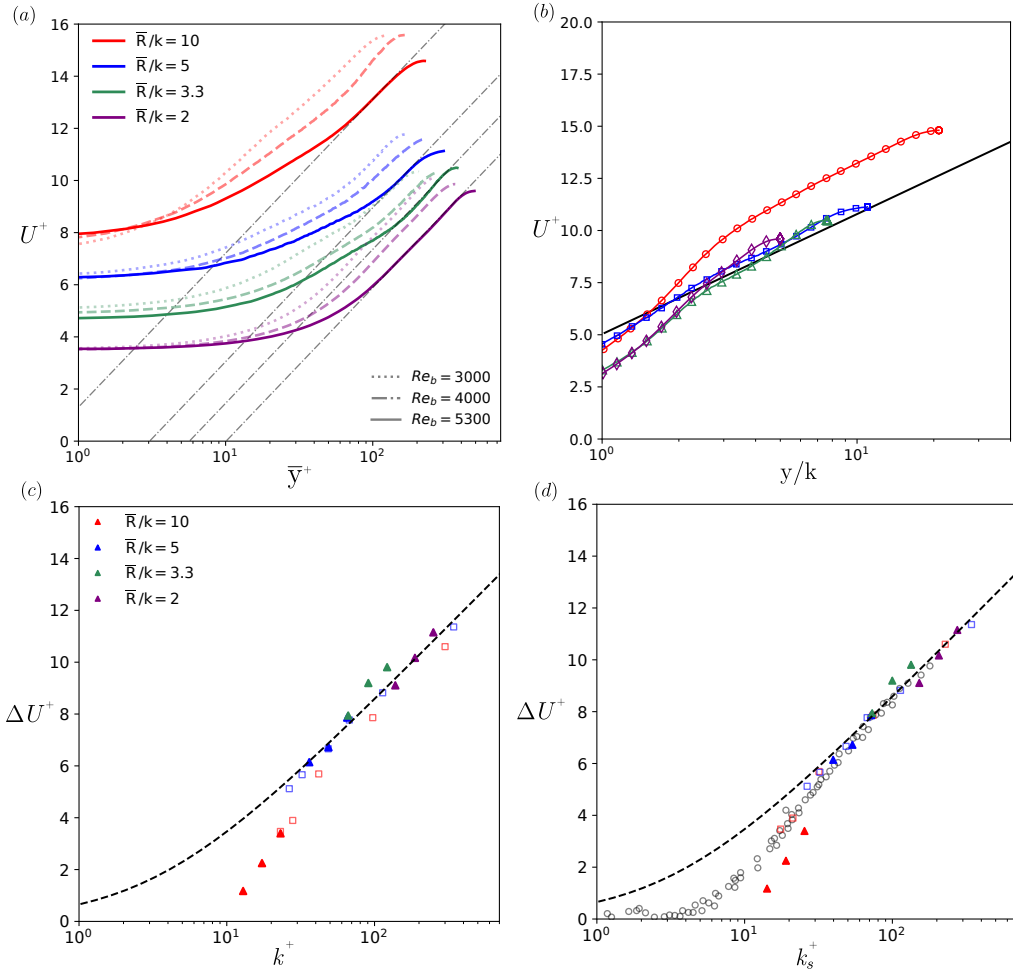


Figure 11. (a) Mean streamwise velocity profiles (U^+) plotted against the wall-normal coordinate (y^+), extracted as the average profiles along the entire pipe length. Results are shown for three bulk Reynolds numbers, $Re_b = 3000, 4000,$ and 5300 , across all investigated roughness levels. (b) Outer-scaled mean velocity profiles for the rough-wall cases at $Re_b = 5300$, plotted as a function of y/k , with $k = H$ wavy full peak to peak distance. (c) Variation of roughness function (ΔU^+) with inner-scaled roughness height ($k^+ = k u_\tau / \nu$) and with equivalent sand-gain roughness height (k_s^+) extracted for for the case reported in (a). As a reference the plots contains empty black circles that represents the data from Nikuradse's experiment. With the squares the De Maio *et al.* (2023) data for the two geometry tested. The dashed line represents the Colebrook's relation (Colebrook *et al.* 1939).

For a given Re_b , increasing wall modulation reduces near-wall and core velocities due to enhanced drag and momentum redistribution. These behaviours are consistent with the roughness-controlled regime described by Flack & Schultz (2014), where surface geometry, not Reynolds number, dominates the flow structure once the roughness scale exceeds a critical threshold. In Figure 11(b), the mean velocity profiles are plotted as a function of the roughness-scaled wall-normal coordinate y/k . For simplicity, only results corresponding to the highest bulk Reynolds number, $Re_b = 5300$, are shown. The profiles approximately collapse onto a single logarithmic trend in the outer region, indicating a self-similar behaviour once scaled with the corrugation amplitude. This confirms that k , defined as the peak-to-peak amplitude of the wall modulation, provides an appropriate characteristic

length scale for wavy-wall flows within the present Reynolds-number range. The observed collapse further suggests that the outer-layer dynamics are predominantly governed by the geometric roughness rather than viscous effects, consistent with a roughness-controlled turbulent regime.

In Figure 11(c), the roughness function ΔU^+ obtained from the simulations is shown as a function of the roughness Reynolds number $k^+ = ku_\tau/\nu$ for different bulk Reynolds numbers ($Re_b = 3000, 4000, \text{ and } 5300$) and roughness levels. The roughness function is computed as the vertical offset between the smooth and rough-wall velocity profiles in the logarithmic region. The smooth reference is taken from simulations at comparable friction Reynolds numbers Re_τ , as in Figure 4(b), allowing consistent comparison despite the non identical wall stress. For reference, data from the rough-pipe simulations of De Maio *et al.* (2023) are also included. The values of ΔU^+ and k^+ obtained for the wavy-pipe cases collapse reasonably well onto the Colebrook relation, confirming that even periodic and deterministic wall geometries produce drag increases comparable to those observed over irregular rough surfaces. For instance, the case with $\bar{R}/k = 2$ and $Re_b = 5300$ yields $\Delta U^+ \approx 11.2$, corresponding to $k^+ \approx 250$, which lies near the upper limit of typical engineering roughness values. Flack & Schultz (2014) reported that most practical rough surfaces fall within $k_s^+ < 800$. The trend observed among the different geometries is consistent with the results of De Maio *et al.* (2023), with roughness functions exceeding $\Delta U^+ = 8$ for the cases with $\bar{R}/k = 3.3$ and 2 , indicating that these flows fall within the strongly fully rough regime. In contrast, for the less wavy geometries, the roughness function remains below this threshold, corresponding to laminar or transitional roughness behaviour within the range of flow conditions investigated, where viscous effects still exert a dominant influence.

An equivalent sand-grain roughness height k_s^+ was estimated by enforcing the universality of the roughness function with respect to the fully rough asymptote represented by the Colebrook relation. Since all geometries examined share the same analytical formulation of the wall modulation, they can be considered part of a single "family of roughness", allowing the data to be fitted collectively. The roughest configuration ($\bar{R}/k = 2, Re_b = 5300$) was taken as the reference case, as it is expected to be the closest to the fully rough regime. From this procedure, an equivalent sand-grain roughness of $k_s^+ \approx 1.1 k^+$ was fitted, indicating that the effective hydraulic roughness is only slightly larger than the geometric amplitude of the corrugation. The resulting comparison, reported in Fig. 11(d), includes data from De Maio *et al.* (2023) and the classical experiments of Nikuradse as reference cases. It may be noted that the results for the other geometries do not collapse perfectly onto the Colebrook curve. This deviation is expected, given that a single case was used as the reference to define the equivalent sand-grain roughness. Introducing separate k_s values for each configuration would likely improve the collapse but would also deviate from the aim of identifying a single, universal scaling. The obtained value, $k_s^+ \approx 1.1 k^+$, reinforces the choice of the geometric amplitude k as the relevant length scale for these wavy-wall geometries, consistent with the self-similar behaviour observed earlier in Figure 11(b).

To further examine the relationship between surface geometry and flow response, the equivalent roughness heights ($k_{s,\text{ref}}^+$) were derived by inverting the Colebrook relation (Clauser 1954; Hama 1954; Jimenez 2004; De Maio *et al.* 2023) using the velocity offset ΔU^+ obtained from the logarithmic region of the simulated mean profiles. These values were then compared with geometric and empirical estimates, as reported in Tab. 2. The analysis was performed for the two geometries at $\bar{R}/k = 3.3$ and $\bar{R}/k = 2$, corresponding to $k_{s,\text{ref}}^+ = 165.2$ and 285.2 , respectively, considering the highest Reynolds number ($Re_b = 5300$). The simplest estimate, which assumes that the flow experiences the full peak-to-peak

Reference	Formula	k_s	k_s^+ (pred.)	k_s^+ (ref.)	Error [%]
Peak to Peak distance	$k_s = k$	0.1304	121.7	165.2	-26.4
		0.2	250.7	285.2	-12.3
Napoli <i>et al.</i> (2008)	$k_s^+ = a^+ [0.772 + ES (2.37 - ES)]$	-	80.4	165.2	-51.3
		-	195.1	285.2	-31.6
Chan <i>et al.</i> (2015)	$k_s = 7.3 S_a ES^{0.45}$	0.166	154.4	165.2	-6.5
		0.308	384.7	285.2	+34.9
Saha <i>et al.</i> (2015)	$k_s = 2k$	0.261	243.4	165.2	+47.3
		0.400	500.1	285.2	+75.4
Forooghi <i>et al.</i> (2017)	$k_s = k (0.67 S_k^2 + 0.93 S_k + 1.3)$ $[1.07 (1 - e^{-3.5 ES})]$	0.109	101.3	165.2	-38.7
		0.210	262.1	285.2	-8.1
Flack & Schultz (2020)	$k_s = 2.11 S_q$	0.097	90.8	165.2	-45.1
		0.149	186.6	285.2	-34.6

Table 2. Estimated equivalent sand-grain roughness heights k_s for the sinusoidal-walled pipe cases at $Re_b = 5300$. Each correlation is evaluated using the geometric peak-to-peak roughness k and wavelength $\lambda = 1$. The two cases correspond to $\bar{R}/k = 3.3$ and $\bar{R}/k = 2$, respectively. The resulting k_s^+ values predicted from the various empirical correlations are compared with those obtained from the logarithmic-law offset ($k_{s,ref}^+$) derived from the simulations. The percentage error is computed relative to the reference $k_{s,ref}^+$ for each case.

roughness height ($k_s = k$), yields $k_s^+ = 122$ and 250 , under predicting the reference values by approximately 26% and 12%. Among the literature correlations considered, those of Chan *et al.* (2015) and Forooghi *et al.* (2017) provide similarly close predictions, while models developed for irregular roughness (Napoli *et al.* 2008; Saha *et al.* 2015; Flack & Schultz 2020) tend to deviate more strongly. Overall, the peak-to-peak definition offers the best agreement across the two cases (total absolute error $\approx 39\%$), suggesting that, for smooth periodic roughness, the geometric amplitude k remains the most physically relevant length scale controlling the drag response.

These results confirm that the wavy geometries considered here operate within the fully rough regime. The consistency with canonical scaling laws, including those of Nikuradse (1933) and Colebrook *et al.* (1939), reinforces the robustness of ΔU^+ and k_s^+ as general descriptors of rough-wall turbulence, even in geometries that are large-scale, deterministic, and spatially coherent. This trend also highlights the limitations of purely geometric characterisations and supports the use of velocity-based metrics as a more reliable, flow-informed measure of equivalent roughness.

Conclusions

This study examined turbulent flow through pipes with sinusoidally wavy walls using direct numerical simulations at moderate Reynolds numbers. The analysis explored how wall amplitude modifies the mean flow and drag, combining classical roughness metrics with inner-scaled velocity profiles. Once the wall modulation becomes strong enough to sustain turbulence, the flow reaches the fully rough regime. The roughness effect generated by the coherent wall shape is more intense than that of the sand-grain or random roughness studied by Nikuradse (1933) and De Maio *et al.* (2023).

In the laminar regime, the friction factor exceeds the Hagen–Poiseuille prediction by 5–40%. This excess disappears only when an effective hydraulic diameter, extracted a

posteriori from the simulated pressure loss, is used to redefine the Reynolds number and friction factor. The increased drag originates from a stable recirculation bubble forming in the expanding half-wave at $Re_b \approx 500$ for $\bar{R}/k \leq 5$. As roughness increases, these recirculations appear at decreasing Reynolds numbers, thickening the near-wall region, displacing high-shear layers towards the core, and promoting an early, geometry-induced transition to turbulence at Reynolds numbers between 500 and 1000 typically assumed for karst conduits (White 2002). That is, the transitions occur well below the threshold for smooth pipes.

Once turbulence is established, the velocity profiles show little sensitivity to Reynolds number and collapse according to roughness level. This behaviour is consistent with the fully rough regime, where pressure drag dominates and the friction factor becomes almost independent of Reynolds number (Jimenez 2004; Flack & Schultz 2014). The reduction in both near-wall and core velocities with increasing amplitude confirms the pressure-driven nature of the flow. Purely geometric estimates of k_s^+ based on wall amplitude and friction velocity tend to underpredict ΔU^+ at high roughness levels, though the discrepancy is modest. The small ratio $k_s^+/k^+ \approx 1.1$ indicates that the geometric peak-to-peak amplitude (k) remains the best single descriptor of roughness in this configuration. The remaining deviation reflects additional form drag, flow separation, and axial pressure gradients, which depend on curvature rather than amplitude alone. Nevertheless, the geometric amplitude captures the main physical contribution to hydraulic roughness.

Overall, the results confirm that ΔU^+ and k_s^+ are reliable descriptors of wall-induced drag once the flow is known. They collapse data across Reynolds numbers and roughness levels, even in structured, non-random geometries. The wavy pipe therefore provides a clean and controllable test case for separating geometric and stochastic effects. Its agreement with classical scaling laws supports the use of deterministic sinusoidal geometries as simplified analogues for complex rough surfaces. At the same time, the findings highlight the limits of predictive models based on a single roughness parameter. Quantities such as k_s^+ , $f(Re)$, or ΔU^+ cannot predict drag a priori when wall shape governs the flow topology. In such cases, axial curvature, expansion and contraction rate, and the spatial organisation of form drag must also be included. Until these multi-parameter models are available, smooth-wall or random-roughness correlations should be used with caution for shape-driven flows.

Acknowledgments

The authors acknowledge funding from the European Union (ERC, KARST, 101071836).

Appendix A. Effect of the averaging region on mean flow statistics

Figure 12 shows the mean streamwise velocity and Reynolds stress profiles obtained by averaging the flow field from the roughness crest (R_{\min}) towards the pipe centreline. This alternative averaging procedure follows the approach of Saha *et al.* (2015) and differs from that adopted in the main text, where statistics were computed over the entire cross-section, including both converging and diverging sections of the wavy geometry. The purpose here is to examine how the definition of the averaging region influences the near-wall behaviour and turbulent structure of the flow, and to allow a consistent comparison with earlier studies on wavy pipes.

Averaging only from the crest has a marked influence on the inner-scaled velocity profiles. By excluding the diverging portions, where the adverse pressure gradient induces local flow reversal and a thickening of the low-speed region, the truncated averages suppress the flattening previously observed near the wall (cf. figure 7). In this representation, the near-

wall velocity rises more sharply and the overall U^+ levels are reduced, particularly within the buffer layer. Because a single global friction velocity (u_τ) is used for normalisation, these changes cannot be attributed to rescaling but instead reflect a genuine redistribution of momentum. The omission of the diverging regions effectively removes zones of separated flow that contribute little to shear production, thereby yielding a more representative depiction of the attached, shear-dominated portion of the boundary layer. The full averages, which include both converging and diverging sections, yield higher U^+ values and a slightly steeper rise in the near-wall region, indicating that locally accelerated flow in the diverging phase augments the mean velocity. Once these regions are excluded, the truncated curves represent a slower, more stable flow confined to the crests and core, with reduced momentum exchange.

The Reynolds shear stress profiles ($\langle u'_r u'_z \rangle^+$) also respond sensitively to the averaging method. Once the diverging regions are excluded, the profiles collapse well into the expected linear distribution of total shear stress, $\tau_w(1 - r/R)$, consistent with canonical turbulent pipe flow. This agreement suggests that the crest-based averaging effectively removes the influence of separated and weak-shear zones, thereby revealing the underlying momentum transfer structure of the attached flow. In the truncated averages, the near-wall peak becomes more pronounced and shifts slightly closer to the wall compared with the full averages. This behaviour arises because the exclusion of recirculating regions eliminates the artificially low-fluctuation zones that otherwise reduce the ensemble-averaged intensity near the wall. As the Reynolds number increases, the peak magnitude grows systematically and the shift towards the wall becomes more evident, consistent with the classical scaling observed in smooth-wall turbulence. In contrast, the full averages display a broader distribution of stress extending further from the wall, which reflects the unsteady separation and reattachment occurring in the diverging regions.

With increasing waviness, and hence decreasing R_{\min} , the difference between the two averaging procedures becomes more pronounced. Overall, these comparisons reveal that the apparent shape of the inner-scaled profiles depends strongly on how the averaging region is defined, and that this sensitivity intensifies with increasing geometric roughness. The truncated averages isolate the shear-driven component of the flow, whereas the full averages capture the combined effects of acceleration and separation intrinsic to the wavy geometry. For consistency, all results presented in the main sections of the paper are based on full averages.

REFERENCES

- AL-DAAMEE, F. Q. & HAMZA, N. H. 2024 Numerical investigation of thermal and entropy generation characteristics in a sinusoidal corrugated channel under the influence of sinusoidal wall temperature. *Int. J. Thermofluids* **22**, 100706.
- BUSSE, A., LÜTZNER, M. & SANDHAM, N. D. 2015 Direct numerical simulation of turbulent flow over a rough surface based on a surface scan. *Comput. Fluids* **116**, 129–147.
- BUSSE, A., THAKKAR, M. & SANDHAM, N. D. 2017 Reynolds-number dependence of the near-wall flow over irregular rough surfaces. *J. Fluid Mech.* **810**.
- CHAN, L., MACDONALD, M., CHUNG, D., HUTCHINS, N. & OOI, A. 2015 A systematic investigation of roughness height and wavelength in turbulent pipe flow in the transitionally rough regime. *J. Fluid Mech.* **771**, 743–777.
- CHUNG, DANIEL, HUTCHINS, NICHOLAS, SCHULTZ, MICHAEL P & FLACK, KAREN A 2021 Predicting the drag of rough surfaces. *Annu. Rev. Fluid Mech.* **53** (1), 439–471.
- CLAUDIN, PHILIPPE, DURÁN, ORENCIO & ANDREOTTI, BRUNO 2017 Dissolution instability and roughening transition. *J. Fluid Mech.* **832**, R2.
- CLAUSER, F. H. 1954 Turbulent boundary layers in adverse pressure gradients. *J. Aero. Sci.* **21**, 91–108.
- COHEN, IRA M & KUNDU, PIJUSH K 2004 *Fluid mechanics*. Elsevier.
- COLEBROOK, C. F., BLENCH, T., CHATLEY, H., ESSEX, E. H., FINNIECOME, J. R., LACEY, G., WILLIAMSON, J. & MACDONALD, G. G. 1939 Correspondence. turbulent flow in pipes, with particular reference to the transition region between the smooth and rough pipe laws (includes plates). *J. Inst. Civil Engrs* **12** (8), 393–422.

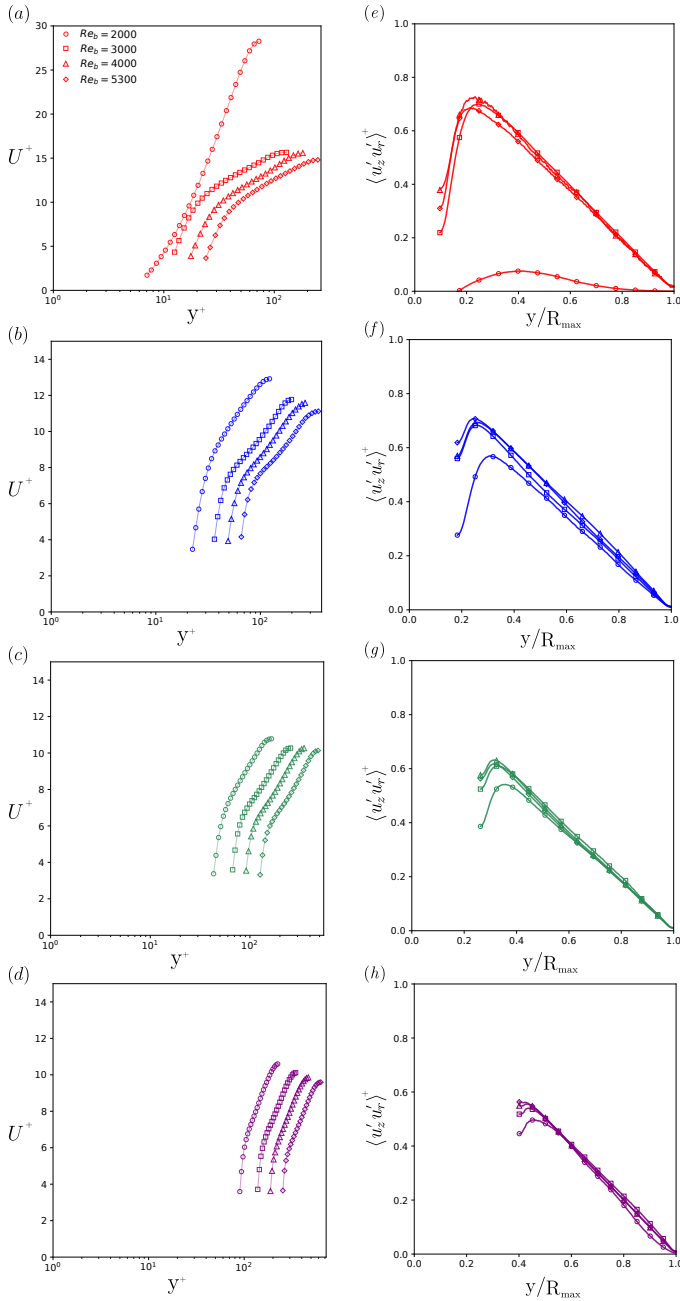


Figure 12. Mean streamwise velocity profiles in inner scaling coordinates (U^+ versus y^+) (a-d), and Reynolds stress profiles in outer scaling coordinates ($\langle u_r' u_z' \rangle^+$ versus y/R_{\max}) (e-h). The panels are arranged in ascending order of surface roughness, from the smoothest to the roughest case (top to bottom). Each curve corresponds to a different bulk Reynolds number, as indicated in panel (a). Profiles are obtained by averaging in the wall-normal direction from the roughness crest towards the pipe centreline.

CURL, RANE L 1966 Caves as a measure of karst. *J. Geol.* **74** (5, Part 2), 798–830.

DE MAIO, M., LATINI, B., NASUTI, F. & PIROZZOLI, S. 2023 Direct numerical simulation of turbulent flow in pipes with realistic large roughness at the wall. *J. Fluid Mech.* **974**, A40.

- DREYBRODT, WOLFGANG 2012 *Processes in karst systems: physics, chemistry, and geology*, vol. 4. Springer Science & Business Media.
- FISCHER, P. F., LOTTES, J. W. & KERKEMEIER, S. G. 2008 Nek5000. <http://nek5000.mcs.anl.gov>.
- FLACK, K. A. & SCHULTZ, M. P. 2014 Roughness effects on wall-bounded turbulent flows. *Phys. Fluids* **32**, 101301.
- FLACK, K. A. & SCHULTZ, M. P. 2020 Skin-friction measurements of systematically-varied roughness. *Flow Turbul. Combust.* **104**, 317–329.
- FLACK, K. A., SCHULTZ, M. P. & SHAPIRO, T. A. 2005 Experimental support for townsend's reynolds number similarity hypothesis on rough walls. *Phys. Fluids* **17**, 035102.
- FOROOGHI, P., STROH, A., MAGAGNATO, F., JAKIRLIĆ, S. & FROHNAPFEL, B. 2017 Towards a universal roughness correlation. *ASME J. Fluids Eng.* **139** (12), 121201.
- GOLDSTEIN, L. JR. & SPARROW, E. M. 1977 Heat/mass transfer characteristics for flow in a corrugated wall channel. *J. Heat Transfer* **99** (2), 187–195.
- GUZMÁN, A. M., CÁRDENAS, M. J., URZÚA, F. A. & ARAYA, P. E. 2009 Heat transfer enhancement by flow bifurcations in asymmetric wavy wall channels. *Int. J. Heat Mass Transfer* **52**, 3778–3789.
- HAMA, F. R. 1954 Boundary-layer characteristics for smooth and rough surfaces. *Trans. Soc. Nav. Archit. Mar. Engrs* **62**, 333–358.
- HSU, S.-T. & KENNEDY, J. F. 1971 Turbulent flow in wavy pipes. *J. Fluid Mech.* **47** (3), 481–502.
- JEANNIN, P. Y. 2001 Modeling flow in phreatic and epiphreatic karst conduits in the Hölloch cave (Muotatal, Switzerland). *Water Resour. Res.* **37** (2), 191–200.
- JIMENEZ, J. 2004 Turbulent flows over rough walls. *Annu. Rev. Fluid Mech.* **36**, 136–196.
- LOH, S. A. & BLACKBURN, H. M. 2011 Stability of steady flow through an axially corrugated pipe. *Phys. Fluids* **23**, 111703.
- MOODY, L. F. 1944 Friction factors for pipe flow. *Transitions of the ASME* **66**, 671–684.
- MOSER, R. D., KIM, J. & MANSOUR, N. N. 1999 Direct numerical simulation of turbulent channel flow up to $\tau = 590$. *Phys. Fluids* **11** (4), 943–945.
- MUSKER, A. J. 1980 Universal roughness functions for naturally-occurring surfaces. *Transactions of the Canadian Society for Mechanical Engineering* **6** (1), 1–6.
- NAPOLI, E., ARMENIO, V. & DE MARCHIS, M. 2008 The effect of the slope of irregularly distributed roughness elements on turbulent wall-bounded flows. *J. Fluid Mech.* **613**, 385–394.
- NIKURADSE, J. 1933 *Strömungsgesetze in rauhen Röhren*. *Forschungshefte de VDI 1*. VDI-Verlag.
- NISHIMURA, T. 1995 Oscillatory flow and mass transfer within asymmetric and symmetric channels with sinusoidal wavy walls. *Heat Mass Transfer* **30**, 269–278.
- NISHIMURA, T., OHORI, Y. & KAWAMURA, Y. 1984 Flow characteristics in a channel with symmetric wavy wall for steady flow. *J. Chem. Eng. of Japan* **17** (5), 466–471.
- PIOMELLI, U. 1993 High reynolds number calculations using the dynamic subgrid-scale stress model. *Phys. Fluids A* **5** (6), 1484–1490.
- PIROZZOLI, P., ROMERO, S., FATICA, M., VERZICCO, R. & ORLANDI, P. 2021 One-point statistics for turbulent pipe flow up to $Re_\tau \approx 6000$. *J. Fluid Mech.* **926**, A28.
- POZRIKIDIS, C. 1987 Creeping flow in two-dimensional channels. *J. Fluid Mech.* **180**, 495–514.
- RAUPACH, MICHAEL R., ANTONIA, ROBERT ANTHONY & RAJAGOPALAN, SUNDARA 1991 Rough-wall turbulent boundary layers. *Appl. Mech. Rev.* **44**, 1–25.
- SAHA, S. K., KLEWICKI, J., OOI, A. P. & BLACKBURN, H. M. 2015 On scaling pipe flows with sinusoidal transversely corrugated walls: Analysis of data from the laminar to the low-reynolds-number turbulent regime. *Journal of Fluid Mechanics* **779**, 245–264.
- SCHLICHTING, H. 1936 Experimentelle untersuchungen zum rauhigkeitsproblem. *Ing.-Arch.* **7**, 1–34.
- SMITH, F. T. 1986 Steady and unsteady boundary-layer separation. *Annu. Rev. Fluid Mech.* **18**, 197–220.
- SUI, Y., TEO, C. J. & LEE, P. S. 2012 Direct numerical simulation of fluid flow and heat transfer in periodic wavy channels with rectangular cross-sections. *Int. J. Heat Mass Transfer* **55**, 73–88.
- THAKKAR, M., BUSSE, A. & SANDHAM, N. 2016 Dataset for surface correlations of hydrodynamic drag for transitionally rough engineering surfaces. <https://eprints.soton.ac.uk/392562/>.
- THAKKAR, M., BUSSE, A. & SANDHAM, N. D. 2018 Direct numerical simulation of turbulent channel flow over a surrogate for nikuradse-type roughness. *J. Fluid Mech.* **837**, R1.
- TOWNSEND, A. A. 1976 *The Structure of Turbulent Shear Flow*, 2nd edn. Cambridge University Press.
- WANG, C.-C. & CHEN, C.-K. 2002 Forced convection in a wavy-wall channel. *Int. J. Heat Mass Transfer* **45**, 2587–2595.
- WANG, G. & VANKA, S. P. 1995 Convective heat transfer in periodic wavy passages. *Int. J. Heat Mass Transfer* **38** (17), 3219–3230.

I. El Mellas, J. J. Hidalgo and M. Dentz

- WANG, L.-P. & DU, M. H. 2008 Direct simulation of viscous flow in a wavy pipe using the lattice boltzmann approach. *Int. J. Eng. Syst. Modelling Simul.* **1** (1), 20–29.
- WHITE, F. M. 2011 *Fluid Mechanics*, 7th edn. McGraw-Hill.
- WHITE, WILLIAM B 2002 Karst hydrology: recent developments and open questions. *Engineering geology* **65** (2-3), 85–105.
- WU, X. & MOIN, P. 2008 A direct numerical simulation study on the mean velocity characteristics in turbulent pipe flow. *J. Fluid Mech.* **608**, 81–112.